Dissecting the neurotropism and neurovirulence of MPXV using human stem cell-based models

Lisa Bauer[1,*], Stefania Giussani[2,*], Nicola Palazzi[2], Farnaz Zare[2], Elisa Colombo[2], Francesca Pinci[2], Lonneke Leijten[1], Hilde Smeenk[3], Carmen W.E. Embregts[1], Malan Silva[2], Jochem K.H. Spoor[4], Clemens Dirven[4], Zhenyu Gao[5], Anne Bolleboom[4,5], Babs E. Verstrepen[1], Leonard Schuele[1], Femke M.S. de Vrij[3,6], Steven A. Kushner[3,7], Bas B. Oude Munnink[1], Jose Davila-Velderrain[2], Debby van Riel[1,#] and Oliver Harschnitz[2,#,§]

[1] Department of Viroscience, Erasmus Medical Center, Rotterdam, The Netherlands

[2] Human Technopole, Viale Rita Levi-Montalcini 1, Milan, Italy

[3] Department of Psychiatry, Erasmus Medical Center, Rotterdam, The Netherlands

[4] Department of Neurosurgery, Erasmus Medical Center, Rotterdam, The Netherlands

[5] Department of Neuroscience, Erasmus Medical Center, Rotterdam, The Netherlands

[6] ENCORE Expertise Center for Neurodevelopmental Disorders, Erasmus Medical Center, Rotterdam, The Netherlands

[7] Department of Psychiatry, Columbia University Irving Medical Center, New York, NY, United States

* These authors contributed equally: Lisa Bauer, Stefania Giussani

# These authors contributed equally: Debby van Riel, Oliver Harschnitz

§ Correspondence: oliver.harschnitz@fht.org (Oliver Harschnitz)

Abstract

Mpox, formerly known as monkeypox, is a zoonotic illness of international concern that can lead to severe disease including neurological sequelae. However, it remains unclear what the neurotropism of monkeypox virus (MPXV) is and how MPXV infection leads to neurological deficits. Here, we determined the neurotropism and neurovirulence of MPXV using human pluripotent stem cell- (hPSC)-derived neural stem cells, astrocytes, cortical neurons, and microglia together with *ex vivo* human brain tissue. We found that MPXV infects and replicates more efficiently in astrocytes and microglia compared to cortical neurons, which unlike glial cells showed activation of distinct antiviral programs that may confer differential susceptibility to MPXV. *Ex vivo* infection of human brain tissue confirmed the susceptibility of astrocytes to MPXV infection, which also had the strongest disease-associated changes. Molecular pathway analyses revealed induction of cellular senescence and a senescence-associated secretory phenotype upon MPXV infection in astrocytes. Finally, we demonstrated that antiviral treatment using tecovirimat inhibits MPXV replication and prevents virus-induced senescence in hPSC-derived astrocytes. Altogether, leveraging hPSC-derived brain cells, we reveal MPXV-induced cell type-specific effects at the molecular and cellular level, which provide important insights into the neuropathogenesis of MPXV infection.

Main text

Mpox, formerly known as monkeypox[1], is an emerging zoonotic disease caused by monkeypox virus (MPXV). Mpox was first described in 1958 in cynomolgus monkeys[2] with the first human case reported in 1970[3]. The double-stranded DNA virus MPXV belongs to the genus *Orthopoxvirus* (family *Poxviridae)* which also includes variola virus, vaccinia virus, and cowpox virus[4]. The clinical presentation and fatality rate associated with MPXV infection depends on the viral clade, among other factors[5,6]. Two distinct clades (clade I and clade II) have been identified and differ in their epidemiological and clinical characteristics, with morbidity and mortality being more pronounced in clade I (10-15% of cases)[4], compared to clade II (0.1-4% of cases)[7,8]. In 2022 mpox cases increased and spread outside areas where it has traditionally been endemic[9]. The threat of MPXV and other orthopoxviruses is high due to the absence of routine smallpox vaccination, as well as the overall lack of knowledge on poxvirus cross-species transmission and the pathogenesis on a host and cellular level[4].

Mpox presents clinically as a systemic illness including fever, myalgia, and a characteristic rash[10,11]. Complications include sepsis, pneumonia, conjunctivitis, and neurological sequelae. In the majority of severe cases, patients present with neuropsychiatric complications including seizures, confusion, and encephalitis, indicating that MPXV is able to invade the central nervous system (CNS)[7,10,12–15]. Despite its severe manifestations, the underlying neuropathogenesis of mpox is unknown, and the susceptibility of different CNS cell types to MPXV infection has not been characterised. Because brain tissue from infected patients is scarce and can only provide insights into the end-phase of the disease, *in vitro* models are necessary to study MPXV neurotropism and neurovirulence in human brain cells.

Hence, we used a human pluripotent stem cell (hPSC)-based platform to systematically evaluate the neurotropic and neurovirulent potential of MPXV in human, disease-relevant CNS cells. Our results suggest a preferential tropism of MPXV for glial cells over cortical neurons.

We identified distinct antiviral responses in neurons and glial, and induction of cellular senescence in astrocytes upon MPXV infection. Lastly, we show that MPXV infection and infection-induced senescence in astrocytes could be ameliorated using antiviral treatment with tecovirimat.

Results

MPXV productively infects human CNS cells. Human PSCs can differentiate into a wide range of brain cells and recapitulate key aspects of CNS function and pathophysiology[16,17]. To study the neurotropism of MPXV (**Fig. S1**), we differentiated hPSCs into pure populations of neural stem cells[18], astrocytes[18] (**Fig. S2a, b**), cortical neurons[19] (**Fig. S2c-j**), and microglia[20] (**Fig. S2k-p**). Human PSCs-derived cells expressed markers of astrocytes (GFAP, S100b, CD44, and SOX9), cortical neurons (FOXG1, MAP2, and CTIP2), or microglia (CX3CR1 and IBA1); validating the differentiation protocols (**Fig. S2**).

To study susceptibility, permissiveness, and response to infection, we inoculated the highly-defined populations of CNS cells with cell-culture propagated clade IIb MPXV at a multiplicity of infection (MOI) of 1. The virus was obtained from a patient isolate of the 2022 outbreak[21] (accession number ON615424.1, European Virus Archive Global) (**Fig. 1a-l**). Immunofluorescence staining revealed that not all CNS populations were equally susceptible to MPXV infection (**Fig. 1a, b, d, e, g, & h**). Astrocytes and microglia were much more susceptible to MPXV infection than cortical neurons, based on MPXV antigen expression. In astrocytes, 74.2% (CI 95% [63.2, 85.2]) of GFAP+ cells were infected at 24 hours post infection (hpi) (**Fig. 1a, b**), increasing to 98.6% (CI 95% [96.6, 100]) at 48 hpi (**Fig. 1b and S3d**). Infection resulted in a severe cytopathic effect, and no astrocytes survived up to 72 hpi. In microglia, 51.8% (CI 95% [42, 61.8]) of IBA1+ cells were infected at 24 hpi, increasing up to 96.4% (CI 95% [92.2, 100]) at 72 hpi (**Fig. 1g, h, Fig. S3f**). In contrast, in MAP2+ cortical

neurons only 9% (CI 95% [3.8, 14.25]) were infected by MPXV at 24 hpi, increasing up to 16.5% (CI 95% [10.6, 22.3]) at 72 hpi (**Fig. 1d, e, Fig S3e**). Neural stem cells were more susceptible than cortical neurons, with 11.5% (CI 95% [6, 16.9]) of infected SOX2+ cells at 24 hpi, 75.3% (CI 95% [57.9, 92.7]) at 48 hpi, and 86.6% (CI 95% [77.7, 95.4]) at 72 hpi (**Fig. S3a-c**). No MPXV antigen was detected in mock-infected cell cultures (**Fig. 1a, d, g**).

To determine the replication efficiency, we collected supernatant daily following MPXV inoculation and performed plaque forming assays on Vero E6 cells. This analysis confirmed productive infection in human astrocytes and microglia at 24, 48, and 72 hpi (**Fig. 1c, i**). No significant increase in viral titer was observed in cortical neurons (to prevent detachment of neuronal cultures, viral inoculate was removed but cells were not washed 1 hour post infection, resulting in a higher viral titer at time point 0, which did not increase over time; **Fig. 1f**). RNA sequencing (RNA-seq) confirmed differences in viral replication efficiency among CNS cells, with the lowest number of viral transcripts detected in cortical neurons compared to astrocytes and microglia at 24 hpi (**Fig. 1j, k**). Unsupervised transmission electron microscopy (TEM) revealed evidence of MPXV assembly at different maturation stages (immature and mature virions) in astrocytes (**Fig. 1l**). Viral particles had a classical pox-like structure and size[4,22]. Virus was not detected by TEM in either cortical neurons or microglia (**Fig. S3g, h**). Together, these results demonstrate that MPXV replicates efficiently in astrocytes and microglia, and to a lesser degree in cortical neurons.

MPXV infects astrocytes in primary human brain tissue. To confirm that astrocytes are susceptible to MPXV infection in conditions resembling *in vivo* physiology**,** we inoculated primary human cortical samples from damaged brains with MPXV ($6*10^5$ and $6*10^6$ PFU). MPXV infection in human astrocytes was observed by co-expression of GFAP and MPXV antigen at 24 hpi. (**Fig. 1m**). No specific staining for MPXV antigen was detected in mock-infected *ex vivo* brain cultures (**Fig. S4a, b**). Furthermore, we observed an increase in viral

titers at 24 hpi, confirming primary human brain cells are both susceptible and permissive to MPXV infection (**Fig. 1n**). These data provide further evidence for the neurotropism of MPXV within the human brain, and confirm the susceptibility of human astrocytes for infection by MPXV.

Transcriptomic analysis of MPXV infected CNS cells. To determine the cell type-specific responses of human brain cells to MPXV infection, we performed RNA-seq of MPXV (MOI = 1, 24 hpi) and mock-infected hPSC-derived astrocytes, cortical neurons, and microglia. Human PSC-derivatives preferentially expressed known marker genes of astrocytes, cortical neurons, or microglia (**Fig. S5a**), and significantly correlated with the transcriptome profiles of their *in vivo* counterparts[23] (**Fig. S5b**), confirming their cellular identity. Principal component analysis (PCA) showed clustering of biological replicates by cell type and treatment group, and suggested a global, cell-type specific transcriptomic shift in response to infection (**Fig. 2a**). Consistent with the cellular phenotypes above (**Fig. 1**), this MPXV-induced transcriptomic shift was much more pronounced in astrocytes than in the other cell types, followed by microglia. Neurons shifted the least (**Fig. 2a-d**). Correlation analysis confirmed these global observations, with significantly lower correlation between infected versus mock transcriptomic signatures in astrocytes than in microglia (average cor = 0.1 astrocytes, 0.53 microglia; p<8e-15, paired two sample t-test) or neurons (average cor = 0.59 neurons; p<8e-16, paired two sample t-test) (**Fig. 2c**). To identify the cell type-specific expression changes driving these trends, we performed differential expression analysis comparing mock versus infected samples for each cell type. Astrocytes showed large-scale transcriptional dysregulation, with a total of 2718 up-regulated and 1711 down-regulated genes (log2 fold change ≥ |1.0|, adjusted $P < 0.01$) (**Fig. 2d**). This was considerably more than in either cortical neurons (655 up-regulated and 275 down-regulated transcripts) or microglia (2059 up-regulated and 1061 down-regulated transcripts) (**Fig. 2d, S5b**). We found relatively little

overlap among up-regulated or down-regulated transcripts in the three different cell types, suggesting a predominantly cell type-specific response to MPXV infection (**Fig. 2e, Fig S5c**). More in-depth analyses revealed distinct differential gene expression patterns among the three cell types, with a subset of genes unique to a single cell type, some differentially expressed genes shared by at least two cell types, and some genes having contrasting patterns of up- or downregulation across cell types (discordant) (**Fig. S5d**). Of note, we also identified a subset of genes that was up-regulated in cortical neurons and down-regulated in glial cells, such as *SERPINE1*, *SIGLEC1*, *ANKRD1*, and *MYOF*, suggesting a potential role for these genes in neuronal antiviral signalling (**Fig. S5e, f**). Genes that were found to be differentially expressed among all three cell-types were involved in inflammatory pathways such as "TNF-alpha signalling via NF-kB", "cellular senescence", and "senescence-associated secretory pathway" (**Fig. S5c**).

MPXV infection inhibits innate antiviral immune response in glial cells. Host cells promote an antiviral state by producing and responding to type I interferon (IFN) through signal transducer and activator of transcription 1 (Stat1)-dependent signalling cascades[24,25]. To characterize the specific effects of MPXV infection on antiviral-related processes, we performed a targeted pathway analysis focusing on Gene Ontology biological processes involved in innate antiviral immunity. We aggregated gene expression values into pathway activity scores and estimated the effect of viral infection on these aggregate scores to perform differential pathway activity analysis (Methods). In homeostatic conditions, most pathways exhibited cell type-specific activity, yet a small subset was active across all three cell types (**Fig. 3a**). In line with cellular phenotypes (**Fig. 1**), MPXV infected astrocytes and microglia displayed a significant down-regulation for innate immune pathway activities, including chemokine production, and type I and II interferon responses (**Fig. 3a, b**). Notably, unlike glial cells, cortical neurons showed a global increase in antiviral-related processes (**Fig. 3a**), with

up-regulation of chemokine and type I interferon production upon MPXV infection. In addition to antiviral processes, we performed a second targeted approach focusing on biological processes involving viral-host interactions. By comparing pathway activity scores in MPXV infected versus uninfected cells, we identified selective down-regulation of pathways involved in the negative regulation of the viral life cycle (e.g. "Negative Regulation of Viral Life Cycle" and "Negative Regulation of Viral Genome Replication"; see boxed selection of processes) in glial cells not observed in neurons (**Fig. 3c, d**). These results suggest brain cell-type specific transcriptional responses to MPXV infection involving innate immunity that may play a role in the increased susceptibility and permissiveness of astrocytes and microglia to MPXV infection and replication.

Glial transcriptional response reflects viral life cycle promotion. Poxvirus cellular tropism is dependent on different virus-host interactions which may affect specific aspects of the viral life cycle. While many viruses rely on receptors for viral binding and entry, no such receptors have been identified for poxviruses to date[4,26], but poxvirus binding and entry can be dependent on glycosaminoglycans and laminins. In homeostatic conditions, astrocytes showed a higher expression of laminins compared to microglia and cortical neurons (**Fig. S6a**). Molecular chaperones, such as heat-shock proteins (HSPs), have been reported to have a direct effect on poxvirus replication by interaction with viral core proteins which are crucial for viral assembly[4,27]. We observed that MPXV infection induced a significant upregulation of HSPs, in particular in glial cells (**Fig. S6b**). Viral egress and actin-based extrusion of poxvirus is regulated by several host proteins[4]. Genes encoding proteins that play a role in poxvirus extrusion (*WASL* and *WIPF3*) were similarly up-regulated upon infection in glial cells (**Fig. S6c**). Together, these data show virus-host interactions involved in the MPXV viral life cycle.

MPXV infection induces cellular senescence in astrocytes. Viral infection may lead to cellular senescence[28,29], also in the brain[30,31], which can result in tissue damage and long-term

deficits. Differential expression and pathway enrichment analysis showed a significant overrepresentation for pathways implicated in "cellular senescence" and "senescence-associated secretory phenotype" ("SASP") in genes overexpressed in MPXV-infected astrocytes (**Fig. 4a**), and differential activity of senescence-associated Reactome pathways (**Fig. 4b**). Senescence-associated genes (e.g., *ETS1*, *ETS2*, *NFKB1,* and *JUN)*, and SASP-associated genes (e.g., *IL1A*, *IL6*, and *CXCL8)* were significantly upregulated in MPXV-infected astrocytes (**Fig. 4c**). qRT-PCR analysis confirmed the upregulation of senescence and SASP-associated genes *NFKB1*, *IL6*, *IL1A*, *CXCL8*, *ETS1*, *ETS2*, and *CDKN2D* and the downregulation of *LMNB1* upon MPXV infection (**Fig. 4d, e**). Multiplexed bead assays for cytokine profiling confirmed the upregulation of infection-induced proinflammatory cytokines IL6 and CXCL8 at a protein level (**Fig. 4f**). Cellular phenotypic assays showed additional senescence-associated phenotypes in MPXV-infected astrocytes, such as an impaired mitochondrial function as indicated by the observation of aberrant mitochondrial networks in Mitotracker staining (**Fig. 4g**)[32], which was supported by our transcriptional profiling that demonstrated significant down-regulation of mitochondria-associated pathways (**Fig. 4h**). Altogether, these data suggest that MPXV infection of astrocytes leads to productive infection, pro-inflammatory cellular responses, and a virus-induced cellular senescence phenotype.

Tecovirimat treatment inhibits MPXV replication and rescues cellular senescence in astrocytes. No specific treatment is currently approved for mpox-encephalitis. Drug sensitivity of smallpox antivirals, such as tecovirimat (Tpoxx) (**Fig. 5a**), has been tested for the circulating MPXV clades in cell lines and primary cultures, such as human foreskin fibroblasts, human foreskin keratinocytes, and kidney organoids[21,33–35]. The efficacy of such antivirals is highly dependent on the model and cell-type used[35], however, and has not been tested in CNS cells. To test the efficacy of Tpoxx to treat mpox-induced CNS cellular pathology, we inoculated hPSC-derived astrocytes with MPXV (MOI = 1), treated cells with serial dilutions of Tpoxx

(0.005-5 μM), and tested for cell viability and antiviral efficacy (**Fig. 5**). We observed no signs of cytotoxicity of astrocytes following 5 μM of Tpoxx treatment (**Fig. 5b, c**), and a significant reduction of viral titers (**Fig. 5d**). This is in line with the mechanism-of-action of tecovirimat, which specifically prevents the production of infectious progeny by inhibiting the VP37 envelope wrapping protein[36,37]. Moreover, Tpoxx treatment led to a reduction in MPXV-infected astrocytes in a concentration-dependent manner. Upon 5 μM Tpoxx treatment, MPXV infection was almost fully prevented (1.6% (CI 95% [0, 3.97]) MPXV+/GFAP+ cells versus 98.0% (CI 95% [94.32, 100]) MPXV+/GFAP+ cells in DMSO treated conditions) at 48 hpi as shown by immunofluorescence staining for MPXV (**Fig. 5e, f**). Finally, expression levels of genes involved in senescence and SASP (*NFKB1*, *IL6*, *IL1A*, *CXCL8*, *ETS1*, *ETS2*, and *CDKN2D*) were restored to physiological levels in tecovirimat treated astrocytes in the presence of MPXV, suggesting that Tpoxx treatment may rescue the molecular effects of MPXV infection in astrocytes. (**Fig. 5g**). Together, these data suggest that Tpoxx inhibits viral replication in human astrocytes and MPXV-induced astrosenescence and could therefore be a potential therapeutic candidate to treat mpox encephalitis.

Discussion

The rise of hPSC-based disease modelling allows the study of emerging pathogens such as SARS-CoV-2 and MPXV in human, disease-relevant cells of the brain[17,38]. Recent work using human organoid models of the gut[39] and kidney[21] has established the tropism of MPXV in these respective organ systems. Using previously established protocols[18–20], we identified that *in vitro* human astrocytes and microglia are more susceptible and permissive to MPXV infection than cortical neurons. This increased susceptibility and permissiveness to MPXV infection of glial cells at a cellular level coincides with an impaired IFN and innate antiviral response at a molecular level after MPXV infection.

We show – in both hPSC models and *ex vivo* brain slices – differences in the tropism of MPXV among CNS cells. The ability of MPXV to replicate efficiently in both astrocytes and microglia fits with its ability to cause severe encephalitis. Cell type-specific susceptibility to viral infection and infection-induced pathology is an important feature of many neurotropic viruses leading to virus-specific clinical phenotypes[17]. Previous work has demonstrated a selective tropism of viruses for various CNS cell types, such as NPCs (Zikavirus[40–43]), trigeminal neurons (Herpes simplex virus-1[44]), dopaminergic neurons (SARS-CoV-2[30]), the choroid plexus (SARS-CoV-2[45–47]), and microglia (Rubella virus[48]). More insights into the neuropathogenesis of mpox, such as its neuroinvasive potential, requires analyses of autopsy brain samples from patients with mpox encephalitis or experimental *in vivo* studies. Furthermore, and follow-up studies using complementary models will further our understanding on the neurotropism and neurovirulence of mpox in the acute and post-acute phase of infection.

Cell type-specific transcriptional responses to MPXV infection were associated with a high susceptibility and permissiveness of glial cells to MPXV infection. Innate antiviral signalling pathways involved in the regulation of IFN production and response to IFNs were up-regulated in cortical neurons but down-regulated in astrocytes and microglia. Binding of IFNs to the IFN-ab receptor (IFNAR) leads to the activation of intracellular signalling and downstream interferon stimulated gene (ISG) expression which is essential for viral restriction. The lack of this response in glial cells is therefore likely associated with the efficient infection and replication of MPXV in glial cells in our *in vitro* and *ex vivo* models. In line with our findings, it has been demonstrated that unique host antiviral programs regulate the differential susceptibility within the brain to neurotropic viruses[49]. Therefore, IFNs may be of potential

therapeutic use to treat viral encephalitis, either as monotherapy or as combination therapy with other antivirals[50,51].

Characterization of the transcriptomic shift occurring in human astrocytes following MPXV infection revealed infection-induced molecular phenotypes that may be associated with cell and tissue damage as well as neurodegeneration. We found that MPXV infection led to cellular senescence and a senescence-associated secretory phenotype in astrocytes. Previous work has indicated that cellular senescence in astrocytes, also known as astrosenescence, can be a precursor to neurodegeneration[52]. So far, the molecular mechanisms through which neurotropic viruses may lead to neurodegenerative disease are unknown, although there is increasing evidence linking viral infection with the risk of neurodegenerative disorders[53–58].

Tpoxx treatment of astrocytes resulted in a partial inhibition of virus replication, strongly reducing the number of infected cells in a concentration-dependent manner. Whether this would be sufficient to suppress viral replication in the brain *in vivo* is unclear, although animal studies have shown that Tpoxx can cross the blood-brain barrier. Our experiments also revealed a rescue of MPXV infection-induced cellular senescence in astrocytes, which may be of importance in preventing long-term neurological deficits that can occur following viral infection.

A potential limitation of our study is the use of highly pure, mono-cultures of hPSC-derived CNS cells. While this allows for the careful dissection of cell-intrinsic responses to MPXV infection, it precludes the study of cell-nonautonomous interactions which can be important in antiviral signalling. The use of more complex co-culture systems, organoid models, and *in vivo*

studies will allow for a better understanding of cell-cell interactions, paracrine signalling, and viral spread.

Overall, our study suggests a broad tropism of MPXV throughout the human brain with a preferential susceptibility of glial cells, including astrocytes, as a key target for MPXV infection. Notably, in stark contrast to neurons, glial cells failed to activate essential innate antiviral signalling cascades upon viral infection. MPXV infection leads to cellular senescence and a senescence-associated secretory phenotype, which in turn may trigger long-term neuropathology. Furthermore, we show that tecovirimat treatment could inhibit viral infection and prevent MPXV-induced senescence. Building on our hPSC-based models and data, future research could investigate the cell-nonautonomous signalling that occurs upon MPXV infection, and the potential risk of developing long-term neurological deficits.

Acknowledgements.

We thank the Genomics Facility, Light Imaging Facility, Cryo-Electron Microscopy Unit, and Flow Cytometry Unit at Human Technopole and the BSL-3 facility of the diagnostic unit of the Viroscience department at Erasmus Medical Center for technical support. We are grateful to members of the Van Riel lab and Harschnitz lab for insightful discussions. We acknowledge funding from the Human Technopole (O.H. and J.D.V.). L.B. is supported by The Netherlands Organization for Scientific Research (XS contract number OCENW.XS22.2.045) and by a grant 2023 from the European Society of Clinical Microbiology and Infectious Diseases (Europäische Gesellschaft für klinische Mikrobiologie und Infektionskrankheiten) (ESCMID). N.P. is a PhD student within the European School of Molecular Medicine (SEMM). E.C. is supported by an EMBO postdoctoral fellowship (EMBO ALTF 418-2022). This work was supported by the Netherlands Organ-on-Chip Initiative, an NWO Gravitation project (024.003.001) funded by the Ministry of Education, Culture and Science of the government of the Netherlands, the ZonMW PSIDER program TAILORED (10250022110002) (S.A.K., F.M.S.D.V.), and by an Erasmus MC Human Disease Model Award (F.M.S.D.V., H.S.). D.V.R. is supported by fellowships from The Netherlands Organization for Scientific Research (VIDI contract 91718308). O.H. is supported by fellowships from the Warren Alpert Foundation and the Brain & Behavior Research Foundation.

Author Contribution.

Conceptualization: O.H. and D.v.R. Methodology: L.B. and S.G. Virus production: L.B., L.L., and B.E.V. Sequencing of viral stocks: L.S. and B.O.-M. MPXV infections: L.B. Cortical neuron differentiation experiments: S.G. and N.P. Microglia differentiation experiments: S.G. and N.P. Astrocyte differentiation experiments: L.B. and H.S. F.M.S.D.V. and S.A.K. designed and supervised astrocyte differentiation experiments. RT-qPCR experiments: F.P. Legendplex experiments: L.B, and C.W.E.E. TEM experiments: S.G. and M.S. RNA-seq and bioinformatics analyses: F.Z. and J.D.V. Primary human brain tissue: J.S. and C.D. Primary human brain tissue cultures: A.B. and Z.G. Imaging and image analysis: L.B., S.G., N.P., and E.C. Writing—original draft: O.H. Writing—review and editing: L.B., S.G., D.v.R., J.D.V., and O.H. All authors discussed and analysed the data. Supervision: D.v.R. and O.H.

Competing Interests.

The authors declare no competing interests.

Main Figures Titles and Legends.

Fig. 1. Astrocytes, cortical neurons, and microglia are differentially susceptible and permissive to MPXV infection. a-b, Immunofluorescence staining for astrocyte protein GFAP (grey) and MPXV antigen (red), with quantification (**b**) of MPXV+/GFAP+ cells. No cells survived up to the 72 hpi timepoint. Images representative of three independent experiments. **c,** Plaque forming assays of supernatant collected from MPXV-infected astrocytes. **d-e,** Immunofluorescence staining for neuronal protein MAP2 (grey) and MPXV antigen (red) with quantification (**e**) of MPXV+/MAP2+ cells. Images representative of three independent experiments. **f,** Plaque forming assays of supernatant collected from MPXV-infected cortical neurons. **g-h,** Immunofluorescence staining for microglial protein IBA1 (grey) and MPXV antigen (red) with quantification (**h**) of MPXV+/IBA1+ cells. Images representative of three independent experiments. **i,** Plaque forming assays of supernatant collected from MPXV-infected microglia. **j,** Normalized viral reads following RNA-seq 24 hours after MPXV infection of astrocytes, cortical neurons, and microglia. **k,** Alignment and distribution of viral reads to the viral genome per cell-type. **l,** MPXV at different stages of its life cycle was detected in astrocytes via EM 24 hpi (scale bar = 5 um). Immature virions (*i*, scale bar = 500 nm; *ii*, scale bar = 200 nm) have a round shape compared to the typical brick-like shape of the mature virus (scale bar = 200 nm). **m**, Three-dimensional reconstruction of a representative image of MPXV-infected human brain slice. GFAP co-staining shows MPOX infection in astrocytes. **n,** Plaque forming assays of MPXV-infected human brain tissue cultures. **a-i,** $n = 3$. Statistical analysis was performed using Kruskal-Wallis one-way ANOVA with Dunn's correction for multiple comparisons. *$p < 0.05$, **$p < 0.01$, ***$p < 0.001$, ****$p < 0.0001$. All data represent mean ± SD from three pooled experiments. All experiments were performed in biological triplicates and three independent experiments were performed.

Fig. 2. MPXV-infected astrocytes show the strongest transcriptional shift compared to microglia and cortical neurons. a, Principal component analysis of mock- and MPXV-infected hPSC-derived astrocytes, cortical neurons, and astrocytes (n = 3 independent samples for each cell type). **b,** Pairwise correlations of transcriptional signatures (samplewise relative expression profiles). **c,** Distribution of transcriptomic similarity values (signature correlation) between mock- and MPXV-infected samples by cell type. **d,** Volcano plot depicting differential expression analysis of mock- vs MPXV-infected hPSC-derived astrocytes, microglia, and cortical neurons. Number of differentially expressed genes (p-adjusted value < 0.01) with a log2 (MPXV/mock fold Change) ≥ |1.0| listed in top corner and colour coded per cell type. **e,** Venn diagram depicting differentially expressed gene overlap among cell types. The area of the circles is in proportion to the size of the gene sets.

Fig. 3. MPXV infection inhibits innate antiviral signalling in glial cells. a, Pathway activity scores for antiviral-associated GO processes. Scores were computed per sample within each cell type. Bottom line plot depicts average per sample activity of all antiviral processes (rows). **b,** Volcano plot depicting differential pathway activity analysis of antiviral-associated GO processes in mock- vs MPXV-infected hPSC-derived astrocytes, microglia, and cortical neurons (adjusted p < 0.05, linear model, mock- versus MPXV-infected). **c-d,** Differential pathway activity analysis for viral-related GO processes depicted as volcano plot (**c**) and differential scores (sign(log[FC]) × –log10[adjusted P]) per cell type (**d**). Boxes highlight processes that are significantly down-regulated (adjusted p < 0.05, linear model, mock- versus MPXV-infected) in astrocytes and microglia as discussed in the main text.

Fig. 4. MPXV-specific induction of senescence and SASP in hPSC-derived astrocytes. a, Representative Reactome Pathways overrepresented in genes with expression changes associated with MPXV-infection in astrocytes (adjusted $P < 0.015$, fast preranked gene set enrichment analysis). **b,** Pathway activity scores for Senescence-associated Reactome pathways with expression changes in mock- versus MPXV-infected astrocytes (p-adjusted value < 0.01, linear model). **c,** Pathway membership (left) and relative expression profiles (right) for Senescence-associated genes differentially expressed in mock- versus MPXV-infected hPSC-derived astrocytes ($n = 3$ independent samples per condition). **d-e,** Reverse transcription quantitative polymerase chain reaction of senescence (**d**) and senescence-associated secretory phenotype (**e**) genes in mock- versus MPXV-infected astrocytes ($n = 2$ independent experiments for each cell type). Statistical analysis was performed using unpaired t-test. All reported p values in the figure are two-sided. $*p < 0.05$, $**p < 0.01$, $***p < 0.001$, $****p < 0.0001$. All data represent mean ± SD. Circles and triangles represent three biological replicates from two independent experiments. **f,** Legendplex quantification of secreted senescence-associated secretory phenotype proteins in mock- versus MPXV-infected astrocytes. Statistical analysis was performed using Kruskal-Wallis one-way ANOVA with Dunn's correction for multiple comparisons. $*p < 0.05$, $**p < 0.01$, $***p < 0.001$, $****p < 0.0001$. Two independent experiments were performed, and all data represent mean ± SEM. **g,** Representative images of mitotracker staining in mock- versus MPXV-infected astrocytes. **h,** Pathway activity scores for mitochondrial Reactome Pathways with differential activity values associated with MPXV-infection in astrocytes (adjusted $p < 0.01$, linear model, mock- versus MPXV-infected).

Fig. 5. Tecovirimat inhibits MPXV replication and rescues MPXV-induced senescence of astrocytes. a, Depiction of the chemical formula of tecovirimat (Tpoxx). **b,** Representative

image of astrocytes treated with 5μM Tpoxx. (scale bar = 100 μm). **c,** Cell viability of astrocytes treated with the corresponding concentration of Tpoxx. **d,** In a single-cycle replication assay, astrocytes were infected with MPXV and treated with a serial dilution of Tpoxx for 48 hrs. Plaque forming assay was used to determine MPXV titers upon Tpoxx treatment. IC50 is indicated. **e,** Astrocytes (GFAP+, grey) were fixed 48 hours post infection and infection was visualised with immunofluorescence staining against MPXV antigen (red). **f,** Infection percentage in astrocytes upon Tpoxx treatment was quantified. **g**, Reverse transcription quantitative polymerase chain reaction of senescence genes in hPSC-derived astrocytes (n = 3 independent samples for each cell type). Statistical analysis was performed using one-way ANOVA with Dunnett's correction for multiple comparisons. *$p < 0.05$, **$p < 0.01$, ***$p < 0.001$, ****$p < 0.0001$. All data represent mean ± SD. Circles and triangles represent three biological replicates from two independent experiments.

Supplementary Figure Titles and Legends.

Fig. S1. Replication kinetic of MPXV in Vero E6 cells. In parallel to infection of human induced pluripotent stem cell derived CNS cells, VeroE6 cells were infected with a multiplicity of infection of 1 as positive control. **a**, Immunofluorescence staining showed an increased amount of MPXV in VeroE6 cells over time. **b**, Titration assay shows an increase of MPXV viral titers over time. All data represent mean ± SD. Every experiment was performed in biological triplicates and three independent experiments were performed.

Fig. S2. Characterization of hPSC-derived NPCs, astrocytes, cortical neurons, and microglia. a-b, Astrocytes were generated by neural progenitor cells and the quality of the differentiation was assessed by immunofluorescence staining for canonical astrocytic markers (GFAP, S100b, SOX9) (scale bar = 20µm). **c-h,** Characterisation of the cortical differentiation by reverse transcription quantitative polymerase chain reaction shows a decrease in stem cell markers (**c, d**) and an increase in neuronal markers (**e, g, h**). Postmitotic cells were obtained, as shown by a decrease in *KI67* expression (**f**). **i-j**, Mature cortical neurons (days *in vitro* [DIV]40) were staining for MAP2 and the cortical layer V marker CTIP2. **k-l**, The quality of microglia differentiation was assessed after 3 days *in vitro* by FACS. At DIV3 microglia were 68.36% positive for the primitive haematopoiesis marker CD235a. **m-n**, The quality of microglia differentiation was assessed after 10 days *in vitro* by FACS. At DIV10 microglia were 67.12% positive for CX3CR1. **o-p,** After 30 days *in vitro*, 100% of the microglia culture was positive to the canonical marker IBA1. Scale bar = 20 um. All data represent mean ± SD from three pooled experiments. All experiments were performed in biological triplicates and three independent experiments were performed.

Fig. S3. hPSC-derived NPCs are susceptible and permissive to MPXV infection.

NPCs were infected with MPXV (MOI=1), and their susceptibility and permissiveness to viral infection was tested 24, 48 and 72 hpi. **a-b,** Immunofluorescence staining for the transcription factor SOX2 (grey) and MPXV antigen (red) with quantification (**c**) of MPXV+/SOX2+ cells. Images representative of three independent experiments. **d,** Plaque forming assays of supernatant collected from MPXV-infected NPCs. **d,** Representative image of MPXV infected astrocytes at 48 hpi. **e**, Representative image of MPXV infected cortical neurons at 48 and 72 hpi. **f**, Representative image of MPXV infected microglia at 48 and 72 hpi. **g**, EM representative image of MPXV infected cortical neurons at 24 hpi (scale bar = 5 um). No virus was detected. **h**, EM Representative image of MPXV infected microglia at 24 hpi (scale bar = 2 um; *i*, scale bar = 1 um). No virus was detected, nevertheless cells developed vacuoles. The magnification in *i* shows that the structures seen in the cell were likely mitochondria and other intracellular bodies. **a-d-e-f**, scale bar = 50 µm. Statistical analysis was performed using Kruskal-Wallis one-way ANOVA with Dunn's correction for multiple comparisons. *$p < 0.05$, **$p < 0.01$, ***$p < 0.001$, ****$p < 0.0001$. All data represent mean ± SD from three pooled experiments. All experiments were performed in biological triplicates and three independent experiments were performed.

Fig. S4. MPXV infection in primary brain tissue. a-b Representative images of mock- and MPXV-infected human brain slices stained for astrocyte protein GFAP (grey) and MPXV antigen (red). Scale bar = 20 µm.

Fig. S5. Comparison of gene expression patterns between different cell types. a. Relative expression profiles for cell type marker genes differentially expressed in mock-infected hPSC-derived CNS cells (n = 3 independent samples per condition). **b.** Distribution of transcriptomic

similarity values (signature correlation) comparing in vivo transcriptomic signatures to our hPSC-derived CNS cell transcriptional signatures. **c.** Venn diagram depicting differentially expressed gene overlap among cell types as in **Fig. 2e.** Pathways with differential activity of specific gene sets from Venn diagram are highlighted. **d,** Relative expression profiles for genes with a unique (left) expression pattern, a shared (middle) pattern amongst at least two cell types, or a discordant (right) expression pattern. **e,** Expression pattern of genes that are up-regulated in neurons and down-regulated in at least one glial cell type. **f,** Differential pathway activity of all genes that follow expression pattern described in (e).

Fig. S6. Virus-host mediated transcriptional changes. a, Schematic of MPXV viral life cycle highlighting specific processes involved in viral entry (i), core uncoating and early transcription (ii), and finally viral egress (iii). **b,** Relative expression profiles (left) for laminin genes expressed in mock-infected hPSC-derived astrocytes, neurons, and microglia. Differential expression profiles (right) show differential expression upon MPXV-infection (n = 3 independent samples per cell type). **c,** Relative expression profiles (left) for molecular chaperone genes expressed in mock-infected hPSC-derived astrocytes, neurons, and microglia. Differential expression profiles (right) show differential expression upon MPXV-infection (n = 3 independent samples per cell type). **d,** Relative expression profiles (left) for genes associated with viral trafficking and egress expressed in mock-infected hPSC-derived astrocytes, neurons, and microglia. Differential expression profiles (right) show differential expression upon MPXV-infection (n = 3 independent samples per cell type).

EEV: Extracellular Enveloped Virus; IEV: Intracellular Enveloped Virus.

Material and Methods

VeroE6 cell culture

VeroE6 (ATCC CRL 1586) cells were maintained in Dulbecco's modified Eagle's medium (DMEM; Lonza) supplemented with 10% fetal calf serum (FCS; Sigma-Aldrich), 10 mM HEPES (Gibco), 1.5 mg/ml sodium bicarbonate (Capricornus Scientific), 2 mM L-Glutamine (Capricorn Scientific), 100 IU/ml penicillin and 100mg/ml streptomycin (Capricornus Scientific). Cells were grown at 37°C in 5% CO2 and cells were passaged at confluency with the use of phosphate- buffered saline (PBS) and trypsin-EDTA (0.05%) (Capricornus Scientific). Cells were routinely checked for mycoplasma.

Viruses

MPXV was isolated from a swab from a pox lesion of a Dutch patient by inoculating VeroE6 cells. The isolate belonging to the clade IIb is available through the European Virus Archive Global Ref-SKU: 010V-04721. From initial virus stock, MPXV was passaged two times by inoculating a confluent layer of VeroE6 cells with a multiplicity of infection of 0.1-0.01 in Advanced DMEM/F-12 (Gibco) supplemented with 10 mM HEPES, Penicillin/Streptomycin and 2mM L-Glutamine and 100 µg/ml primocin (Invivogen). The cells were harvested after 3-4 days when full cytopathic effect was observed. Residual cells were scraped off the flask and the lysate were centrifuged 2000x*g* for 2 min. The supernatant was discarded, and the pellet was resuspended in OptiMEM (Gibco) and subjected to three times freeze thaw cycles in a dry-ice ethanol bath. The lysate was diluted in 20 ml Opti-MEM and spun down. The cell debris was discarded, and the supernatant was used for plaque assay and next-generation sequencing.

All MPXV stock propagation and experiments were performed in a Class II Biosafety Cabinet under BSL-3 conditions.

DNA extraction

For amplicon sequencing of MPXV stocks, 110 µL of sample material was centrifuged at 10,000 *xg* for 5 min and 100 µL of supernatant was treated with Turbo DNase (Invitrogen) for 30 min at 37 °C. Nucleic acids were extracted using the High Pure Viral Nucleic Acid Kit (Roche) according to the manufacturer's recommendations.

Amplicon sequencing and data analysis

Multiplex PCR was performed as described previously (https://www.protocols.io/view/monkeypox-virus-whole-genome-sequencing-using-comb-n2bvj6155lk5/v1). Sequencing libraries were prepared using the Ligation Sequencing Kit (SQK-LSK110) (Oxford Nanopore Technologies) with Native Barcode Expansion (EXP-NBD196) (ONT) and sequenced on a GRIDIon (ONT). Reads were basecalled with Guppy v6.0.1 in high accuracy mode, demultiplexed using Porechop v0.2.4 (https://github.com/rrwick/Porechop) and mapped against ON563414.3 using Minimap2 v2.17 (https://github.com/lh3/minimap2). NextClade v2.7.0 was used for sequence quality checks, clade assignment and mutation calling[59]. Consensus sequences were aligned using MAFFT v7.475[60].

RT-qPCR

60 µL of sample was lysed in 90 µL of MagnaPure LC Lysis buffer (Roche) followed by a 30-min incubation with 50 µL Agencourt AMPure XP beads (Beckman Coulter). Beads were washed thrice with 70% ethanol on a DynaMag-96 magnet (Invitrogen) and eluted in 50 µL diethylpyrocarbonate treated water. After extraction, equal amounts of RNA from each sample were used for cDNA synthesis with the kit Revertaid First Strand cDNA synthesis Kit (Thermo Scientific). The obtained cDNA was diluted to 2-4 ng/µl for subsequent qPCR with the Sybr Green (Applied Biosystems) method. qPCR primers have been selected from the Origene Website or designed with different bioinformatic tools (sequences are reported in the table below). For the analysis, the 2^(-ΔΔCt) method was adopted and the expression of genes of interest was normalised to the UBC housekeeping gene. Of note, several possible housekeeping genes were tested in RT-qPCR. All of them came out 2-3.5 cycles later in infected samples compared to mock. We chose UBC because this effect was limited to 2 cycles of difference. We believe that this global effect could be due to the viral RNA being transcribed by infected cells, therefore limiting access of the host genes to the transcription machinery, leading to overall decrease of host transcripts compared to mock samples.

Target	Primers (5’ to 3’)
UBC	Fwd CCGGGATTTGGGTCGCAG Rev TCACGAAGATCTGCATTGTCAAG
ETS1	Fwd GAGTCAACCCAGCCTATCCAGA Rev GAGCGTCTGATAGGACTCTGTG
ETS2	Fwd ACTCCGCCAACTGTGAATTGCC Rev CCACTGGCATACCTGTTGCTCA
LMNB1	Fwd GAGAGCAACATGATGCCCAAGTG Rev GTTCTTCCCTGGCACTGTTGAC
NFKB1	Fwd GCAGCACTACTTCTTGACCACC Rev TCTGCTCCTGAGCATTGACGTC

IGFPB7	Fwd GCCATCACCCAGGTCAGCAAG Rev GGATTCCGATGACCTCACAGCT
IL6	Fwd AGTGAGGAACAAGCCAGAGC Rev TGAGATGAGTTGTCATGTCCTG
CXCL8	Fwd GACCCCAAGGAAAACTGGGTGC Rev TGGCAACCCTACAACAGACCCA
IL1A	Fwd TGTATGTGACTGCCCAAGATGAAG Rev AGAGGAGGTTGGTCTCACTACC

Replication kinetics

Before infection of NPCs, astrocytes, cortical neurons, and microglia, supernatant was removed, and cells were infected with MPXV at an MOI = 1. As control, VeroE6 cells were infected with MPXV also at MOI = 1. After 1 h of incubation at 37°C, the inoculum was removed and NPCs, astrocytes, microglia and VeroE6 cells were washed three times with PBS and fresh cell specific medium was added. Also, in cortical neurons the inoculum was removed and without washing, fresh cortical neuron specific medium was added to prevent cell detachment. At the indicated time points, an aliquot of the supernatant was collected for subsequent analysis. All experiments were performed in biological triplicates.

Plaque assay

For infectivity measurement, VeroE6 cells were seeded at 250.000 cells/well and incubated at 37°C in 5% CO2 overnight. Ten-fold serial dilutions of the collected supernatant in Advanced DMEM/F-12 (Gibco) supplemented with 10 mM HEPES (Gibco), Penicillin/Streptomycin (Capricorn Scientific) and 2mM L-Glutamine (Capricorn Scientific) were added to a monolayer of VeroE6 cells. After incubation at 37°C for 1 hour, the medium was taken off and cells were overlayed with 1.2% Avicel (FMC biopolymers) in Opti-MEM I (1X) + GlutaMAX.

After 48 hours cells were fixed for 30 minutes in formalin and the whole plate was submerged in ice cold 100% ethanol. Cells were washed once with PBS followed by staining with 0.2% Crystal Violet (Sigma) in 20% Methanol (Sigma). Endpoint titers were calculated by visualising plaques using light microscopy and plaque forming units/ml were calculated.

Differentiation of cortical neurons

Cortical neuron differentiations were performed using a previously established protocol using H9 hPSCs (WAe009-A)[19]. Human PSCs were maintained on vitronectin (Thermo Fisher Scientific) at 37°C in 5% CO2 with Essential 8 medium (E8) and passaged once a week with EDTA. Prior to differentiation, hPSCs were dissociated into a single-cell suspension using Accutase and plated at 300,000 cells/cm2 onto geltrex-coated plates in E8 with ROCK inhibitor (R&D; Y-27632; 10 μM). Neural induction was achieved through dual-SMAD inhibition[61] using Essential 6 Medium containing LDN193189 (Stemgent, 100 nM) and SB431542 (R&D, 10 μM), in combination with Wnt inhibition for 3 days. From day 11 onwards, medium was changed to a neural differentiation medium (1:1 DMEM/F12 and Neurobasal, 1× N2 supplement, 1× B27, 1× penicillin/streptomycin). At day 20, neural progenitor cells were either cryopreserved using Stem Cell Banker or replated onto poly-ornithine/laminin/fibronectin plates at 150,000 cells/cm2 in maturation medium. From day 21 onwards, media change occurred every 5 days until day 40, when cortical neurons were used for subsequent experiments.

Differentiation of astrocytes

Human astrocyte differentiations were performed from NPCs that were made according to an embryoid-based protocol[62], from the WTC-11 human iPSC line (provided by Bruce R. Conklin (The Gladstone Institutes and UCSF)). In brief, NPCs were purified using fluorescence-activated cell sorting, according to a previously published protocol[63]. They were further differentiated to astrocytes through addition of 10 ng/ml BMP4 (Abcam) and 10 ng/ml LIF (Tebu Bio) to the NPC medium. The purity of astrocytes was assessed by GFAP and S100b staining.

Differentiation of microglia

Microglia were differentiated according to a previously published protocol using H9 hPSCs[20] (WA099-e). In brief, primitive haematopoiesis was induced through a careful modulation of Wnt signalling. To achieve this, hPSCs were exposed on day 0 to the Wnt activator CHIR99021 (R&D, 3 µm), which was replaced with the Wnt inhibitor IWP2 (Tocris, 2 µm) after 18 hours. The quality of the differentiation was assessed before replating cells on day 3, when the expression of the CD235a marker of primitive haematopoiesis was quantified by flow cytometry (Table 1). Human PSC-derived hemangioblasts were provided the developmental cues needed to give rise to primitive erythromyeloid progenitors (EMPs) by day 10. The quality of the differentiation at this stage was tested by quantifying the expression of CX3CR1 by flow cytometry (Table 1). EMPs were subjected to M-CSF (R&D, 10 ng/ml) and IL34 (R&D, 100 ng/ml) to obtain mature microglia on day 30, when they were used for viral experiments. The quality of the differentiation was tested by immunofluorescence staining for the microglial marker IBA1.

Immunofluorescence staining

Cells were fixed with 10% formalin for 30 minutes at room temperature. Cells were permeabilized with 1% Triton-X (Sigma Aldrich) in PBS for 15 minutes on room temperature followed by a blocking step with blocking buffer (PBS supplemented with 1% BSA (Sigma Aldrich) and 0.5% Triton-X (Sigma Aldrich)) for 30 minutes on room temperature. The SOX2 antibody was pre-conjugated overnight with Zenon™ Rabbit IgG Labeling Kits Alexa-647 (Invitrogen, Z25308). Primary antibody incubation was performed overnight at room temperature in blocking buffer. Cells were washed three times in PBS and secondary antibody incubation was performed in blocking buffer for 1 hr at room temperature. To visualise cell nuclei, cells were incubated with a solution of Hoechst (Invitrogen, H3570) which was added during secondary antibody incubation. Slides were washed in PBS, dipped in water and mounted in ProLong Antifade Mountant (Thermo Fisher). Samples were imaged using a Zeiss LSM 700 confocal microscope.

Table 1. Antibodies used for stainings.

Antibody	**Dilution**	**Manufacturer**	**Cat #**	**Lot**
SOX2	1:100	Millipore	AB5603	3254559
MAP2	1:200	Synaptic Systems	188004	30021200
GFAP	1:200	BD Pharma	556327	2277814
GFAP (ex vivo staining)	1:100	Invitrogen	14-9892-82	

Vaccinia Virus Lister-FITC	1:1000	Abbexa	abx022301	
IBA-1	1:200	Abcam	AB5076	
CD235a - APC	1:400	BD	551336	
CX3CR1 - 421	1:100	Biolegend	341619	
donkey anti mouse AF555	1:1000	Invitrogen	A31570	2153958
donkey anti mouse AF647	1:1000		A31571	2311820
goat anti guinea pig AF647	1:1000		A21450	2110845

Mitotracker staining

To evaluate the appearance and distribution of mitochondria we used the MitoTracker™ Red CMXRos (Invitrogen, M7512). Mitotracker powder was diluted in DMSO to a 1 mM stock concentration. Prior to adding the dye to the infected MPXV cells, it was diluted to 500 nM in astrocyte medium. Cells were incubated with the dye for 45 minutes at 37°C. After incubation the cells were fixed for 30 minutes in formalin and taken out of the BSL3 lab. After washing the cells three times with PBS, cells were permeabilized and stained for intracellular markers as described in immunofluorescence staining section.

Multiplexed bead assay for cytokine profiling

Cytokines were measured using the LEGENDplex human antivirus response panel (BioLegend). The kit was used according to the manufacturer's manual with an additional fixing step. After adding the SA-PE and performing the washing steps, the supernatant and the beads were fixed with formalin for 15 min at room temperature and washed twice with the provided wash buffer. This ensures that all pathogens are not infectious.

Patient material for human brain slices

Human brain tissue was used after approval of the Medical Ethical Committee of the Erasmus University Medical Center (protocol MEC-2022-0776). Written informed consent was obtained prior to surgery in accordance with the Declaration of Helsinki. Tissue samples were obtained from patients undergoing brain tumour surgery at the Department of Neurosurgery (Erasmus University Medical Centre Rotterdam, the Netherlands). Infiltrated peri-tumoral neocortical specimens were removed during the regular course of tumour resection. Human patient samples were anonymised manually.

Acute brain slice preparation

Immediately after resection, human peritumoral cortex was placed in ice-cold oxygenated (95%O2/5%CO2) artificial cerebrospinal fluid (aCSF) containing (in mM): 124 NaCl, 24 NaHCO3, 22 D-glucose, 2.5 KCl, 1.25 NaH2PO4, 2 MgSO4, and 2 CaCl2. 350 um thick coronal slices were prepared on a vibratome (VT1200S, Leica) in oxygenated (95%O2/5% CO2) ice-cold N-methyl-d-glucamine (NMDG)-based slicing solution containing (in mM): 93 NMDG, 93 HCl, 25 D-glucose, 30 NaHCO3, 2.5 KCl, 0.5 CaCl2, 10 MgCl2, 20 HEPES, 1.25

NaH2PO4, 12 N-acetyl-cysteine, 2 thiourea, 5 Na-ascorbate, 3 Na-pyruvate (300 mOsm, pH 7.4).

Infection of human brain slices

350 micron thick brain slices from the cortical regions were transferred into 12-well trans-well inserts (Corning). The apical compartment and the basolateral compartment were filled with cortical neuron medium. The brain slices were infected with an equivalent of 1*10^5 or 1*10^6 PFU of MPXV in the apical compartments. After 1 hour of incubation, brain slices were washed once with PBS and fresh medium was added. 24 hrs after infection, supernatant was removed and wells were filled with 10% formalin and cells were fixed for 3 days at room temperature.

Staining of *ex vivo* human brain slices

After fixation, brain slices were transferred in PBS with 30% sucrose until fully immersed, embedded in OCT compound (Scigen), frozen rapidly, and stored at −20°C. Fifteen-micrometre-thick sections were sliced on a cryostat (Leica). For immunofluorescence staining, brain slices were rinsed in PBS, incubated with Retrieval Solution (Dako) for 45 minutes at 70°C, permeabilized with 0,5% Triton X-100 in PBS1x for 20 minutes, and blocked with 0,1% Triton X-100, 10% Donkey Serum in PBS1x for 1 hour at room temperature. Afterwards the brain sections were incubated with Mouse α GFAP (Table 1) and Rabbit α Vaccinia Virus Lister Strain FITC (Table 1) overnight. After washing, mouse primary antibody was visualised with 1:1000 Donkey α Mouse Alexa Fluor™ Plus 647 (Invitrogen, A32787) or 1:1000 Donkey α Mouse Alexa Fluor™ Plus 555 (Invitrogen, A32773). Nuclei were stained with DAPI

(Thermo Fisher, 62248). Immunostained sections were scanned using confocal microscope LSM 980 (Zeiss), with objective magnification of 40x and 63x, (16 bits, frame size 2048 pixels x 2048 pixels).

Tecovirimat rescue experiments

MPXV infection was performed by incubating a confluent layer of hPSC-derived astrocytes at a MOI 1 for 1 hour at 37 °C. Next, supernatant was removed, and cells were washed three times with PBS. After the washing steps, fresh astrocyte medium with a serial dilution of tecovirimat (Selleckchem) was added to the cells. At the indicated timepoints, medium was collected to determine virus titers by plaque assay, cells were fixed to determine the infection percentage by immunofluorescence staining, or cells were lysed for RNA isolation at indicated timepoints. Tecovirimat was dissolved in DMSO at 10mM stock concentration and stored at -20°C. Cell viability was measured with an CellTiter-Glo® Luminescent Cell Viability Assay (Promega) and values were compared to mock treatment. The concentration of compound that inhibits plaque forming units by 50% (IC50) was calculated by nonlinear regression analysis with GraphPad Prism Version 10.

Transmission electron microscopy

Fixation of Sapphires.

Cortical neurons, astrocytes and microglia were plated on 6 mm diameter, 120 um thin sapphire disks containing a 15 nm thick evaporated gold patterning and coated with poly-L ornithine, fibronectin and laminin, and infected with an MOI=1. After 24 hrs, the cells were gently rinsed three times with the corresponding cell medium and cells were fixed with 2.5% glutaraldehyde

in 0.1M sodium cacodylate buffer, pH 7.4 for 1 hour at room temperature. Subsequently, the cells were fixed with 10% formalin for 30 minutes at room temperature. The formalin was replaced with 1,2% of Glutaraldehyde and 4% Formaldehyde and fixed cells were stored at 4°C until further processing.

Sample preparation and acquisition.

Cells on the sapphire disk were high-pressure frozen using Leica EM ICE high-pressure freezer. Samples were subsequently freeze-substituted in 0.1% uranyl acetate in acetone containing 2% water at -90°C for 40 hrs in a Leica AFS2 freeze substitution device. Cells were warmed to -45°C over 10 hrs before washing twice with acetone. Cells were progressively infiltrated with UV-curable Lowicryl HM20 resin (Electron Microscopy Sciences), starting at -45°C and ending at -25°C over 25 hrs. Infiltrated samples were exposed to diffused UV radiation for 48 hrs at -25°C. Samples were warmed to room temperature at +1.5°C /hr steps with continuous UV exposure. Leica FSP was used for some solution exchange steps. Serial sections (250nm in thickness) were prepared on a Leica UC7 Ultramicrotome and collected onto slot grids with carbon-coated formvar film (Agar Scientific). Sections were not post-stained. Imaging was performed on a Thermo Scientific Spectra 300 S/TEM operated at 300 kV for both STEM and TEM modes. HAADF STEM images were acquired on a Fischione Model 3000 detector at camera length of 275mm, with microscope operating with a 2.8mrad semi-convergence angle and 120pA probe current. STEM imaging and image processing was performed using Thermo Scientific Velox software. TEM tilt series were acquired as 2x2 montages on bottom-mounted Thermo Scientific Ceta-S camera using SerialEM software[64]. Tilt series were aligned, binned by two, and processed into montaged tomograms using the IMOD software package[65].

RNA sequencing

Infections were performed at an MOI of 1 and samples were harvested 24 hpi. Total RNA was extracted using the RNeasy Mini kit (Qiagen) following the on column DNAse digestion protocol, according to manufacturer's instructions. RNA-seq libraries of polyadenylated RNA were prepared using Illumina Stranded mRNA Prep (Illumina) according to the manufacturer's instructions and sequenced on an NovaSeq 6000 PE100 (Illumina).

Paired-end reads were aligned to the human genome reference GRCh38.p13 with the R software package Rsubread[66]. Alignment BAM files were merged using Samtools (1.14-python-3.9.10) when needed. Mapped reads were summarised to gene level counts with the featureCounts function of Rsubread, using reference gene annotations (v.42) downloaded from the GENECODE project (https://www.gencodegenes.org/human/). Protein coding genes with detected counts in at least one sample library were retained and normalized using TMM normalization. For viral read mapping the same procedure was followed, using the Monkeypox virus genome (Genbank No.ON563414.3) and annotation as reference.

Differential expression and pathway enrichment analysis.

Differential expression analysis was performed with the edgeR package. Genes with a FDR-corrected $P < 0.01$ and an absolute log2 fold change (FC) > 1.0 were considered as differentially expressed. Differential expression analysis results for all cell types are reported in Supplementary Tables. Gene ontology and functional enrichment analyses were performed

using Fast Gene Set Enrichment Analysis (fgsea) for ranked gene lists and Enrichr (https://maayanlab.cloud/Enrichr/) and gprofiler2 (https://cran.r-project.org/web/packages/gprofiler2/index.html) for gene sets. Statistical analyses and plots were performed using the programming language R (R Core Team, 2012).

Pathway activity scores and differential pathway activity analysis

Pathway activity scores were calculated for each RNAseq sample by gene set variation analysis as implemented in the R package GSVA (v.1.42.0). Briefly, GSVA estimates a normalized relative expression level per gene across samples. This expression level is then rank-ordered for each sample and aggregated into gene set or pathway scores by calculating sample-wise enrichment using a Kolmogorov–Smirnov-like rank statistic. Antiviral related pathways (GO:0035455, GO:0035456, GO:0034341, GO:0034340, GO:0032647, GO:0032648, GO:0032649, GO:0032479, GO:0034097, GO:0001817, GO:1990868, GO:0032642) were extracted from GO Biological Processes v2023 downloaded from https://maayanlab.cloud/Enrichr/#libraries, considering terms involving innate immunity, interferon, interleukin, cytokine, and chemokine. Viral related pathways (GO:0044827, GO:0044788, GO:0044828, GO:0044793, GO:0043922, GO:0045869, GO:0045071, GO:1903901, GO:0048525, GO:0032897, GO:0039532, GO:0044829, GO:0044794, GO:0043923, GO:0046598, GO:0045070, GO:1903902, GO:0048524, GO:0045091, GO:0046596, GO:0045069, GO:1903900, GO:0046782, GO:0039531, GO:0044790, GO:0046784) were extracted by filtering Gene Ontology biological processes containing the keyword “viral.” Senescence-associated pathways (R-HSA-2559582, R-HSA-2559583, R-HSA-2559580) were extracted from the Reactome Pathway Database v2022 by filtering

pathways containing the keyword “senescence.” Differential pathway activity analysis was performed for each pathway-cell type combination by testing for an association between pathway activity scores and infection status using a linear model and computing t-statistics as implemented in the lmfit() and eBayes() functions from the Limma R package (v.3.50.3).

Statistical analysis

Statistical analysis was performed as explained in detail in the figure legends with the latest available version of GraphPad Prism.

References

1. Ulaeto, D. *et al.* New nomenclature for mpox (monkeypox) and monkeypox virus clades. *Lancet Infect. Dis.* **23**, 273–275 (2023).
2. Magnus, P. von, Andersen, E. K., Petersen, K. B. & Birch-Andersen, A. A pox-like disease in Cynomolgus monkeys. *Acta Pathol. Microbiol. Scand.* **46**, 156–176 (2009).
3. Parker, S. & Buller, R. M. A review of experimental and natural infections of animals with monkeypox virus between 1958 and 2012. *Future Virol.* **8**, 129–157 (2013).
4. McFadden, G. Poxvirus tropism. *Nat. Rev. Microbiol.* **3**, 201–213 (2005).
5. Likos, A. M. *et al.* A tale of two clades: monkeypox viruses. *J. Gen. Virol.* **86**, 2661–2672 (2005).
6. Americo, J. L., Earl, P. L. & Moss, B. Virulence differences of mpox (monkeypox) virus clades I, IIa, and IIb.1 in a small animal model. *Proc. Natl. Acad. Sci. U. S. A.* **120**, e2220415120 (2023).
7. Badenoch, J. B. *et al.* Neurological and psychiatric presentations associated with human monkeypox virus infection: A systematic review and meta-analysis. *EClinicalMedicine* **52**, 101644 (2022).
8. Adler, H. *et al.* Clinical features and management of human monkeypox: a retrospective observational study in the UK. *Lancet Infect. Dis.* **22**, 1153–1162 (2022).
9. Thornhill, J. P. *et al.* Monkeypox Virus Infection in Humans across 16 Countries - April-June 2022. *N. Engl. J. Med.* **387**, 679–691 (2022).
10. Fink, D. L. *et al.* Clinical features and management of individuals admitted to hospital with monkeypox and associated complications across the UK: a retrospective cohort study. *Lancet Infect. Dis.* (2022) doi:10.1016/S1473-3099(22)00806-4.
11. Thornhill, J. P. *et al.* Human monkeypox virus infection in women and non-binary individuals during the 2022 outbreaks: a global case series. *Lancet* **400**, 1953–1965

(2022).

12. Cole, J. *et al.* Monkeypox encephalitis with transverse myelitis in a female patient. *Lancet Infect. Dis.* (2022) doi:10.1016/S1473-3099(22)00741-1.
13. Billioux, B. J., Mbaya, O. T., Sejvar, J. & Nath, A. Neurologic Complications of Smallpox and Monkeypox: A Review. *JAMA Neurol.* (2022) doi:10.1001/jamaneurol.2022.3491.
14. Pastula, D. M. & Tyler, K. L. An overview of monkeypox virus and its neuroinvasive potential. *Ann. Neurol.* (2022) doi:10.1002/ana.26473.
15. Sharma, R., Nguyen-Luu, T., Dhaubhadel, P., Sharma, A. & Naik, R. A rare co-occurrence of Monkeypox encephalitis and neurosyphilis. *Cureus* (2023) doi:10.7759/cureus.35945.
16. Grant Rowe, R. & Daley, G. Q. Induced pluripotent stem cells in disease modelling and drug discovery. *Nat. Rev. Genet.* 1 (2019).
17. Harschnitz, O. & Studer, L. Human stem cell models to study host–virus interactions in the central nervous system. *Nat. Rev. Immunol.* 1–13 (2021).
18. Lendemeijer, B. *et al.* Rapid specification of human pluripotent stem cells to functional astrocytes. *bioRxiv* 2022.08.25.505166 (2022) doi:10.1101/2022.08.25.505166.
19. Ciceri, G. *et al.* An epigenetic barrier sets the timing of human neuronal maturation. *bioRxiv* 2022.06.02.490114 (2022) doi:10.1101/2022.06.02.490114.
20. Guttikonda, S. R. *et al.* Fully defined human pluripotent stem cell-derived microglia and tri-culture system model C3 production in Alzheimer's disease. *Nat. Neurosci.* 1–12 (2021).
21. Li, P. *et al.* Mpox virus infects and injures human kidney organoids, but responding to antiviral treatment. *Cell Discov* **9**, 34 (2023).
22. Müller, M. *et al.* Electron microscopy images of monkeypox virus infection in 24-year-

old man. *Lancet* **400**, 1618 (2022).

23. Zhang, Y. *et al.* Purification and Characterization of Progenitor and Mature Human Astrocytes Reveals Transcriptional and Functional Differences with Mouse. *Neuron* **89**, 37–53 (2016).
24. Ivashkiv, L. B. & Donlin, L. T. Regulation of type I interferon responses. *Nat. Rev. Immunol.* **14**, 36–49 (2014).
25. McNab, F., Mayer-Barber, K., Sher, A., Wack, A. & O'Garra, A. Type I interferons in infectious disease. *Nat. Rev. Immunol.* **15**, 87–103 (2015).
26. Moss, B. Poxvirus cell entry: how many proteins does it take? *Viruses* **4**, 688–707 (2012).
27. Hung, J.-J., Chung, C.-S. & Chang, W. Molecular Chaperone Hsp90 Is Important for Vaccinia Virus Growth in Cells. *J. Virol.* **76**, 1379 (2002).
28. Lee, S. *et al.* Virus-induced senescence is driver and therapeutic target in COVID-19. *Nature* 1–11 (2021).
29. Gioia, U. *et al.* SARS-CoV-2 infection induces DNA damage, through CHK1 degradation and impaired 53BP1 recruitment, and cellular senescence. *Nat. Cell Biol.* 1–15 (2023).
30. Chen, S. *et al.* SARS-CoV-2 Infection Causes Dopaminergic Neuron Senescence. *Res Sq* (2021) doi:10.21203/rs.3.rs-513461/v1.
31. Sivasubramanian, M. K. *et al.* Herpes Simplex Virus Type 1 Preferentially Enhances Neuro-Inflammation and Senescence in Brainstem of Female Mice. *J. Virol.* **96**, e0108122 (2022).
32. Sato, H. *et al.* Downregulation of mitochondrial biogenesis by virus infection triggers antiviral responses by cyclic GMP-AMP synthase. *PLoS Pathog.* **17**, e1009841 (2021).
33. Frenois-Veyrat, G. *et al.* Tecovirimat is effective against human monkeypox virus in

vitro at nanomolar concentrations. *Nat Microbiol* **7**, 1951–1955 (2022).

34. Warner, B. M. *et al.* In vitro and in vivo efficacy of tecovirimat against a recently emerged 2022 monkeypox virus isolate. *Sci. Transl. Med.* **14**, eade7646 (2022).
35. Bojkova, D. *et al.* Drug Sensitivity of Currently Circulating Mpox Viruses. *N. Engl. J. Med.* (2022) doi:10.1056/NEJMc2212136.
36. Yang, G. *et al.* An orally bioavailable antipoxvirus compound (ST-246) inhibits extracellular virus formation and protects mice from lethal orthopoxvirus Challenge. *J. Virol.* **79**, 13139–13149 (2005).
37. Grosenbach, D. W., Jordan, R. & Hruby, D. E. Development of the small-molecule antiviral ST-246 as a smallpox therapeutic. *Future Virol.* **6**, 653–671 (2011).
38. Bauer, L. *et al.* The neuroinvasiveness, neurotropism, and neurovirulence of SARS-CoV-2. *Trends Neurosci.* (2022) doi:10.1016/j.tins.2022.02.006.
39. Watanabe, Y. *et al.* Virological characterization of the 2022 outbreak-causing monkeypox virus using human keratinocytes and colon organoids. *J. Med. Virol.* **95**, e28827 (2023).
40. Qian, X. *et al.* Brain-Region-Specific Organoids Using Mini-bioreactors for Modeling ZIKV Exposure. *Cell* **165**, 1238–1254 (2016).
41. Tang, H. *et al.* Zika Virus Infects Human Cortical Neural Progenitors and Attenuates Their Growth. *Cell Stem Cell* **18**, 587–590 (2016).
42. Cugola, F. R. *et al.* The Brazilian Zika virus strain causes birth defects in experimental models. *Nature* **534**, 267–271 (2016).
43. Garcez, P. P. *et al.* Zika virus impairs growth in human neurospheres and brain organoids. *Science* **352**, 816–818 (2016).
44. Zimmer, B. *et al.* Human iPSC-derived trigeminal neurons lack constitutive TLR3-dependent immunity that protects cortical neurons from HSV-1 infection. *Proc. Natl.*

Acad. Sci. U. S. A. **115**, E8775–E8782 (2018).

45. Pellegrini, L. *et al.* SARS-CoV-2 infects the brain choroid plexus and disrupts the blood-CSF-barrier in human brain organoids. *Cell Stem Cell* (2020) doi:10.1016/j.stem.2020.10.001.
46. Jacob, F. *et al.* Human Pluripotent Stem Cell-Derived Neural Cells and Brain Organoids Reveal SARS-CoV-2 Neurotropism Predominates in Choroid Plexus Epithelium. *Cell Stem Cell* **0**, (2020).
47. Yang, A. C. *et al.* Dysregulation of brain and choroid plexus cell types in severe COVID-19. *Nature* 1–10 (2021).
48. Popova, G. *et al.* Rubella virus tropism and single cell responses in human primary tissue and microglia-containing organoids. *eLife* (2023) doi:10.7554/elife.87696.
49. Cho, H. *et al.* Differential innate immune response programs in neuronal subtypes determine susceptibility to infection in the brain by positive-stranded RNA viruses. *Nat. Med.* **19**, 458–464 (2013).
50. Kalil, A. C. *et al.* Use of interferon-alpha in patients with West Nile encephalitis: report of 2 cases. *Clin. Infect. Dis.* **40**, 764–766 (2005).
51. Wintergerst, U. & Belohradsky, B. H. Acyclovir monotherapy versus acyclovir plus beta-interferon in focal viral encephalitis in children. *Infection* **20**, 207–212 (1992).
52. Cohen, J. & Torres, C. Astrocyte senescence: Evidence and significance. *Aging Cell* **18**, e12937 (2019).
53. Zhou, L., Miranda-Saksena, M. & Saksena, N. K. Viruses and neurodegeneration. *Virol. J.* **10**, 172 (2013).
54. Piacentini, R. *et al.* Herpes Simplex Virus type-1 infection induces synaptic dysfunction in cultured cortical neurons via GSK-3 activation and intraneuronal amyloid-β protein accumulation. *Sci. Rep.* **5**, 15444 (2015).

55. Cairns, D. M. *et al.* A 3D human brain–like tissue model of herpes-induced Alzheimer's disease. *Science Advances* **6**, eaay8828 (2020).

56. Marcocci, M. E. *et al.* Herpes Simplex Virus-1 in the Brain: The Dark Side of a Sneaky Infection. *Trends Microbiol.* (2020) doi:10.1016/j.tim.2020.03.003.

57. Fulton, C. D. M., Beasley, D. W. C., Bente, D. A. & Dineley, K. T. Long-term, West Nile virus-induced neurological changes: A comparison of patients and rodent models. *Brain Behav Immun Health* **7**, 100105 (2020).

58. Levine, K. S. *et al.* Virus exposure and neurodegenerative disease risk across national biobanks. *Neuron* **0**, (2023).

59. Aksamentov, I., Roemer, C., Hodcroft, E. B. & Neher, R. A. Nextclade: clade assignment, mutation calling and quality control for viral genomes. J Open Source Softw 6: 3773. Preprint at (2021).

60. Katoh, K. & Standley, D. M. MAFFT multiple sequence alignment software version 7: improvements in performance and usability. *Mol. Biol. Evol.* **30**, 772–780 (2013).

61. Chambers, S. M. *et al.* Highly efficient neural conversion of human ES and iPS cells by dual inhibition of SMAD signaling. *Nat. Biotechnol.* **27**, 275–280 (2009).

62. Gunhanlar, N. *et al.* A simplified protocol for differentiation of electrophysiologically mature neuronal networks from human induced pluripotent stem cells. *Mol. Psychiatry* **23**, 1336–1344 (2018).

63. Yuan, S. H. *et al.* Cell-surface marker signatures for the isolation of neural stem cells, glia and neurons derived from human pluripotent stem cells. *PLoS One* **6**, e17540 (2011).

64. Mastronarde, D. N. SerialEM: A Program for Automated Tilt Series Acquisition on Tecnai Microscopes Using Prediction of Specimen Position. *Microsc. Microanal.* **9**, 1182–1183 (2003).

65. Kremer, J. R., Mastronarde, D. N. & McIntosh, J. R. Computer visualization of three-dimensional image data using IMOD. *J. Struct. Biol.* **116**, 71–76 (1996).

66. Liao, Y., Smyth, G. K. & Shi, W. The R package Rsubread is easier, faster, cheaper and better for alignment and quantification of RNA sequencing reads. *Nucleic Acids Res.* **47**, e47 (2019).

Figure 1

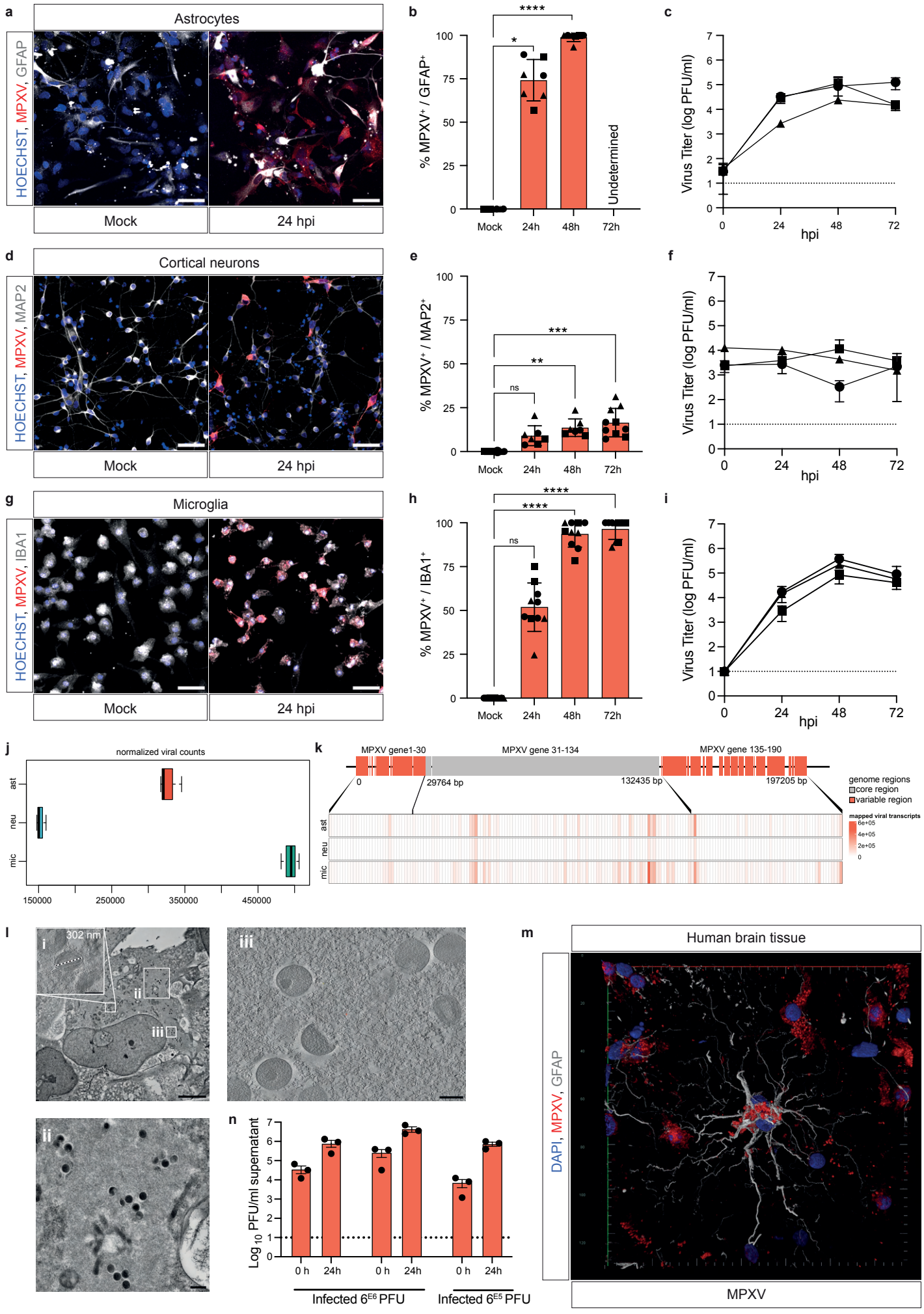
a
Astrocytes
HOECHST, MPXV, GFAP
Mock
24 hpi
b
% MPXV+ / GFAP+
Undetermined
Mock
24h
48h
72h
c
Virus Titer (log PFU/ml)
hpi
d
Cortical neurons
HOECHST, MPXV, MAP2
e
% MPXV+ / MAP2+
ns
f
g
Microglia
HOECHST, MPXV, IBA1
h
% MPXV+ / IBA1+
i
j
normalized viral counts
ast
neu
mic
k
MPXV gene1-30
MPXV gene 31-134
MPXV gene 135-190
29764 bp
132435 bp
197205 bp
genome regions
core region
variable region
mapped viral transcripts
l
302 nm
i
ii
iii
n
Log10 PFU/ml supernatant
0 h
24h
Infected 6E6 PFU
Infected 6E5 PFU
m
Human brain tissue
DAPI, MPXV, GFAP
MPXV

Figure 2

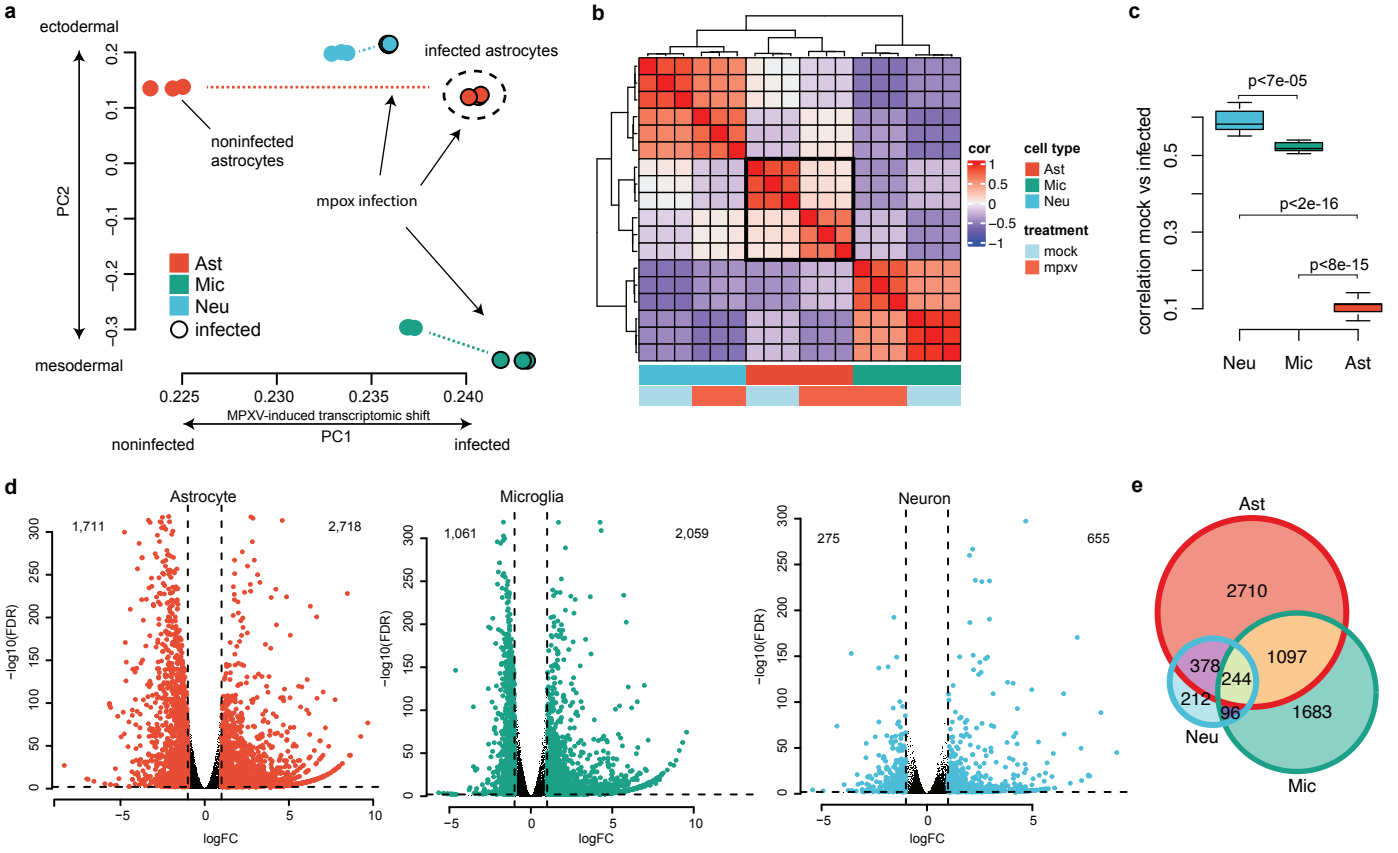
a
ectodermal
mesodermal
PC2
0.2
0.1
0.0
−0.1
−0.2
−0.3
infected astrocytes
noninfected astrocytes
mpox infection
Ast
Mic
Neu
infected
0.225
0.230
0.235
0.240
MPXV-induced transcriptomic shift
noninfected
PC1
infected
b
cor
1
0.5
0
−0.5
−1
cell type
Ast
Mic
Neu
treatment
mock
mpxv
c
p<7e-05
p<2e-16
p<8e-15
correlation mock vs infected
0.1
0.3
0.5
Neu
Mic
Ast
d
Astrocyte
1,711
2,718
Microglia
1,061
2,059
Neuron
275
655
−log10(FDR)
logFC
e
Ast
2710
1097
378
244
212
96
1683
Neu
Mic

Figure 3

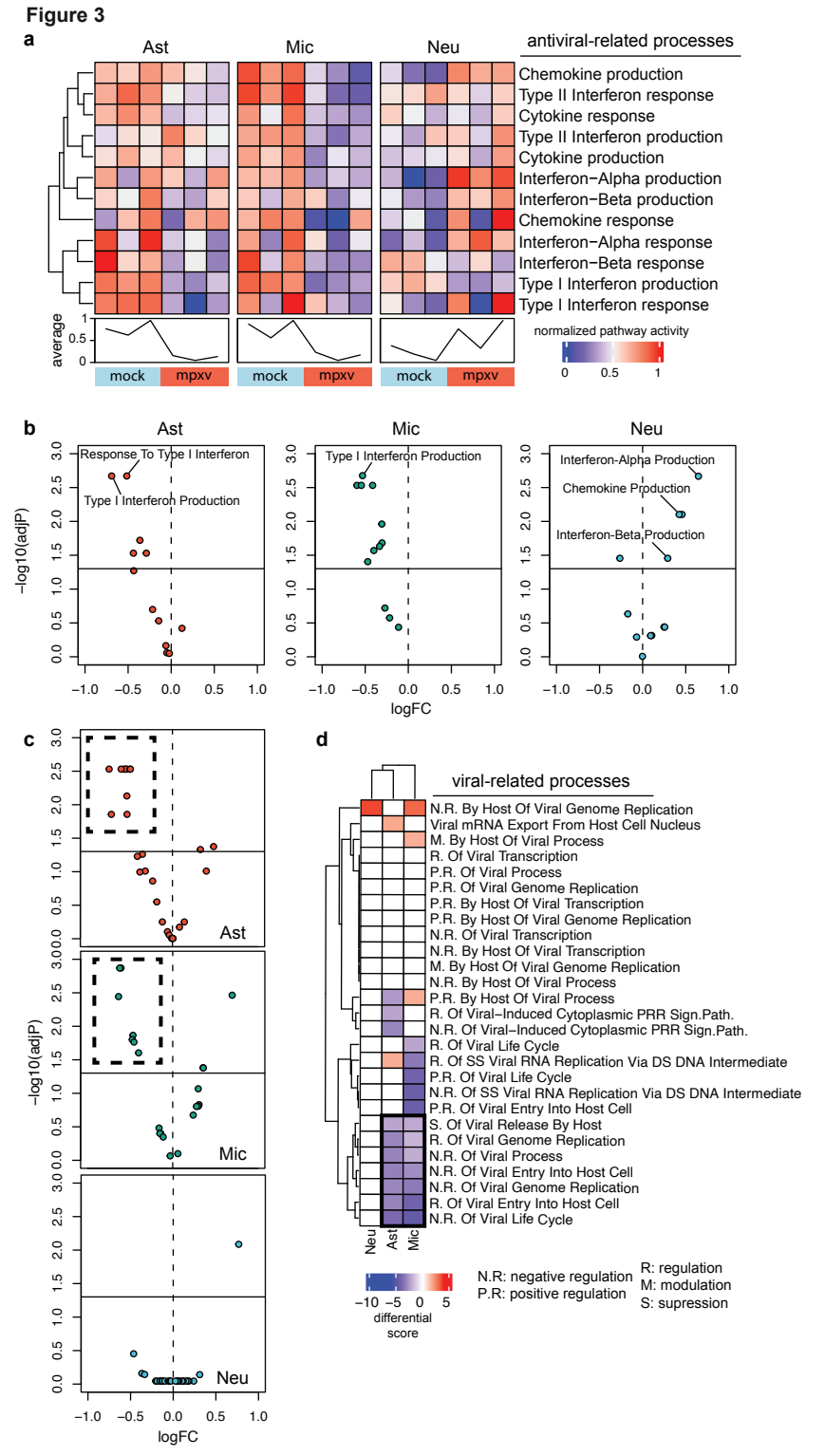
a
Ast
Mic
Neu
antiviral-related processes
Chemokine production
Type II Interferon response
Cytokine response
Type II Interferon production
Cytokine production
Interferon−Alpha production
Interferon−Beta production
Chemokine response
Interferon−Alpha response
Interferon−Beta response
Type I Interferon production
Type I Interferon response
average
mock
mpxv
normalized pathway activity
b
Response To Type I Interferon
Type I Interferon Production
Interferon-Alpha Production
Chemokine Production
Interferon-Beta Production
−log10(adjP)
logFC
c
d
viral-related processes
N.R. By Host Of Viral Genome Replication
Viral mRNA Export From Host Cell Nucleus
M. By Host Of Viral Process
R. Of Viral Transcription
P.R. Of Viral Process
P.R. Of Viral Genome Replication
P.R. By Host Of Viral Transcription
P.R. By Host Of Viral Genome Replication
N.R. Of Viral Transcription
N.R. By Host Of Viral Transcription
M. By Host Of Viral Genome Replication
N.R. By Host Of Viral Process
P.R. By Host Of Viral Process
R. Of Viral−Induced Cytoplasmic PRR Sign.Path.
N.R. Of Viral−Induced Cytoplasmic PRR Sign.Path.
R. Of Viral Life Cycle
R. Of SS Viral RNA Replication Via DS DNA Intermediate
P.R. Of Viral Life Cycle
N.R. Of SS Viral RNA Replication Via DS DNA Intermediate
P.R. Of Viral Entry Into Host Cell
S. Of Viral Release By Host
R. Of Viral Genome Replication
N.R. Of Viral Process
N.R. Of Viral Entry Into Host Cell
N.R. Of Viral Genome Replication
R. Of Viral Entry Into Host Cell
N.R. Of Viral Life Cycle
Neu
Ast
Mic
differential score
N.R: negative regulation
P.R: positive regulation
R: regulation
M: modulation
S: supression

Figure 4

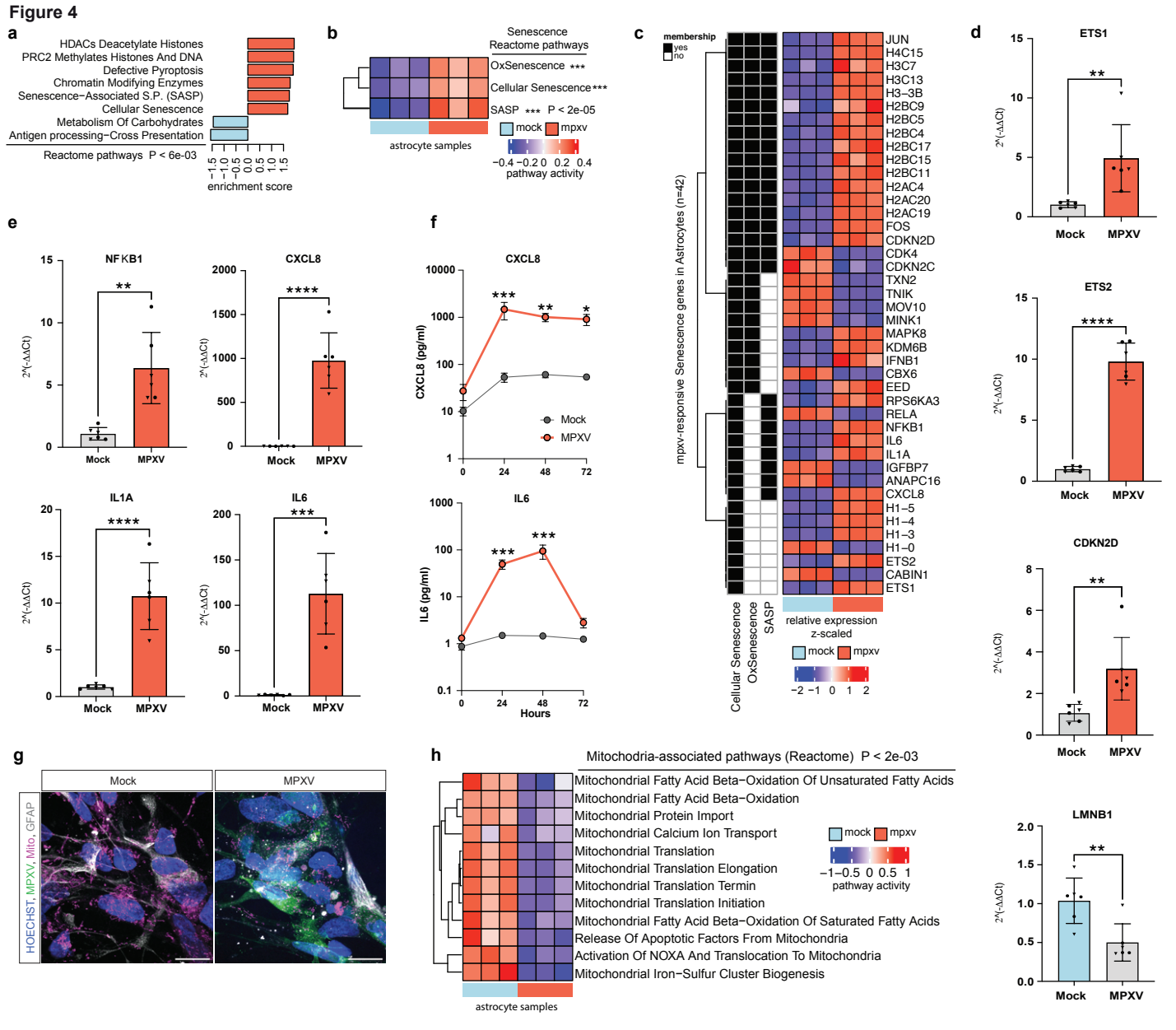
a
HDACs Deacetylate Histones
PRC2 Methylates Histones And DNA
Defective Pyroptosis
Chromatin Modifying Enzymes
Senescence−Associated S.P. (SASP)
Cellular Senescence
Metabolism Of Carbohydrates
Antigen processing−Cross Presentation
Reactome pathways P < 6e-03
−1.5 −1.0 −0.5 0.0 0.5 1.0 1.5
enrichment score
b
Senescence Reactome pathways
OxSenescence ***
Cellular Senescence***
SASP *** P < 2e-05
mock mpxv
astrocyte samples
−0.4 −0.2 0 0.2 0.4
pathway activity
c
membership
yes
no
mpxv-responsive Senescence genes in Astrocytes (n=42)
JUN
H4C15
H3C7
H3C13
H3−3B
H2BC9
H2BC5
H2BC4
H2BC17
H2BC15
H2BC11
H2AC4
H2AC20
H2AC19
FOS
CDKN2D
CDK4
CDKN2C
TXN2
TNIK
MOV10
MINK1
MAPK8
KDM6B
IFNB1
CBX6
EED
RPS6KA3
RELA
NFKB1
IL6
IL1A
IGFBP7
ANAPC16
CXCL8
H1−5
H1−4
H1−3
H1−0
ETS2
CABIN1
ETS1
Cellular Senescence
OxSenescence
SASP
relative expression z-scaled
mock mpxv
−2 −1 0 1 2
d
ETS1
ETS2
CDKN2D
LMNB1
2^(-ΔΔCt)
Mock
MPXV
e
NFKB1
CXCL8
IL1A
IL6
2^(-ΔΔCt)
Mock
MPXV
f
CXCL8
IL6
CXCL8 (pg/ml)
IL6 (pg/ml)
Mock
MPXV
Hours
g
Mock
MPXV
HOECHST, MPXV, Mito, GFAP
h
Mitochodria-associated pathways (Reactome) P < 2e-03
Mitochondrial Fatty Acid Beta−Oxidation Of Unsaturated Fatty Acids
Mitochondrial Fatty Acid Beta−Oxidation
Mitochondrial Protein Import
Mitochondrial Calcium Ion Transport
Mitochondrial Translation
Mitochondrial Translation Elongation
Mitochondrial Translation Termin
Mitochondrial Translation Initiation
Mitochondrial Fatty Acid Beta−Oxidation Of Saturated Fatty Acids
Release Of Apoptotic Factors From Mitochondria
Activation Of NOXA And Translocation To Mitochondria
Mitochondrial Iron−Sulfur Cluster Biogenesis
mock mpxv
−1 −0.5 0 0.5 1
pathway activity
astrocyte samples

Figure 5

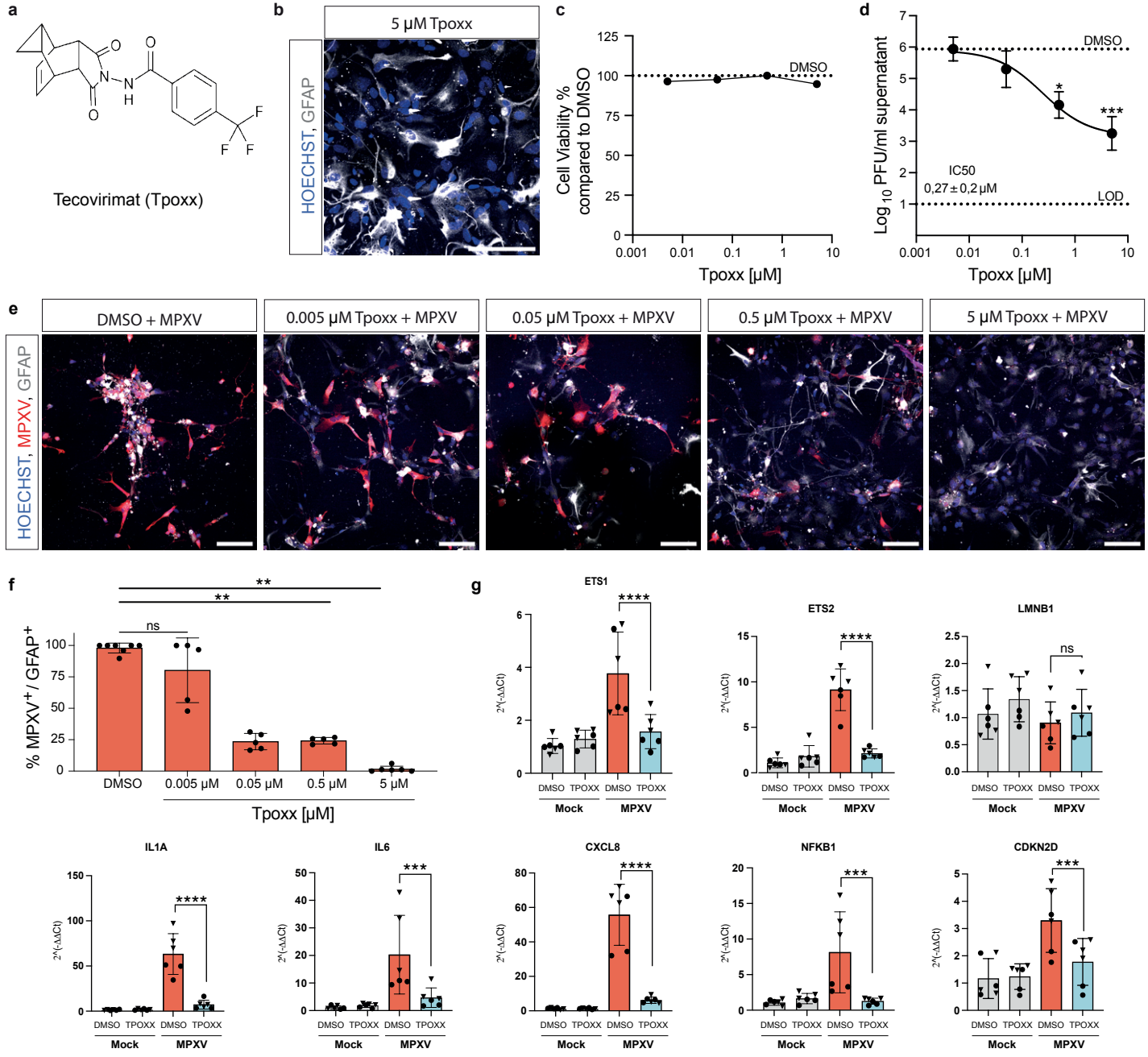
a
Tecovirimat (Tpoxx)
b
5 µM Tpoxx
HOECHST, GFAP
c
Cell Viability % compared to DMSO
DMSO
Tpoxx [µM]
d
Log 10 PFU/ml supernatant
DMSO
IC50
0,27 ± 0,2 µM
LOD
Tpoxx [µM]
e
DMSO + MPXV
0.005 µM Tpoxx + MPXV
0.05 µM Tpoxx + MPXV
0.5 µM Tpoxx + MPXV
5 µM Tpoxx + MPXV
HOECHST, MPXV, GFAP
f
% MPXV+ / GFAP+
ns
DMSO
0.005 µM
0.05 µM
0.5 µM
5 µM
Tpoxx [µM]
g
ETS1
ETS2
LMNB1
IL1A
IL6
CXCL8
NFKB1
CDKN2D
2^(-ΔΔCt)
DMSO
TPOXX
Mock
MPXV

Supplementary figure 1

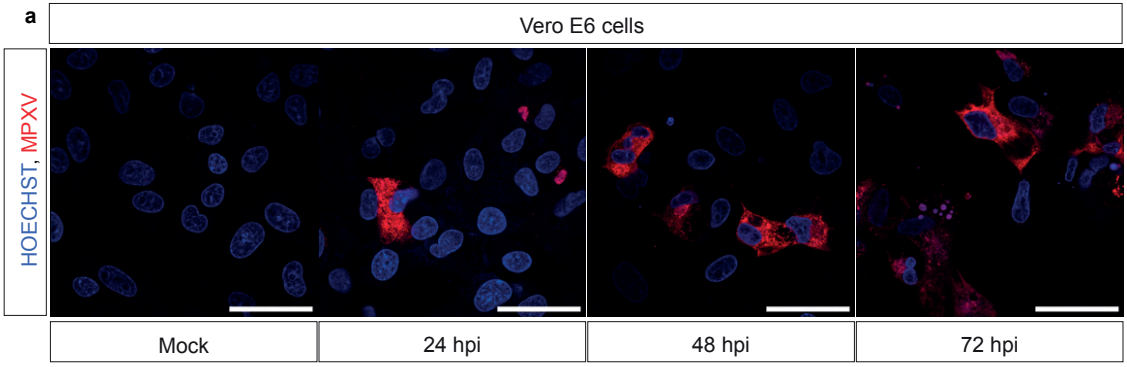

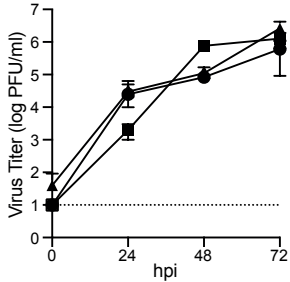

Supplementary figure 2

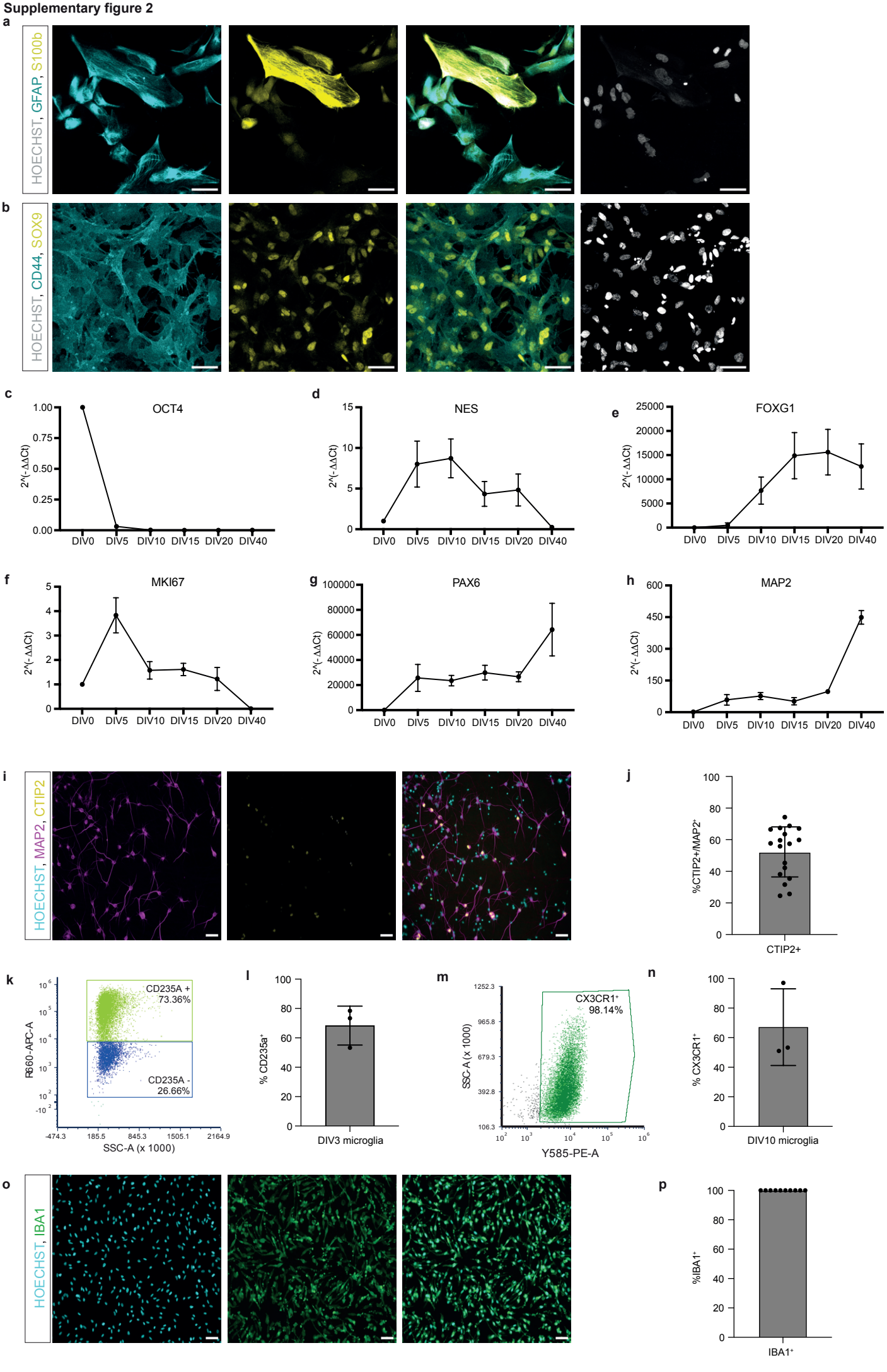

Supplementary figure 3

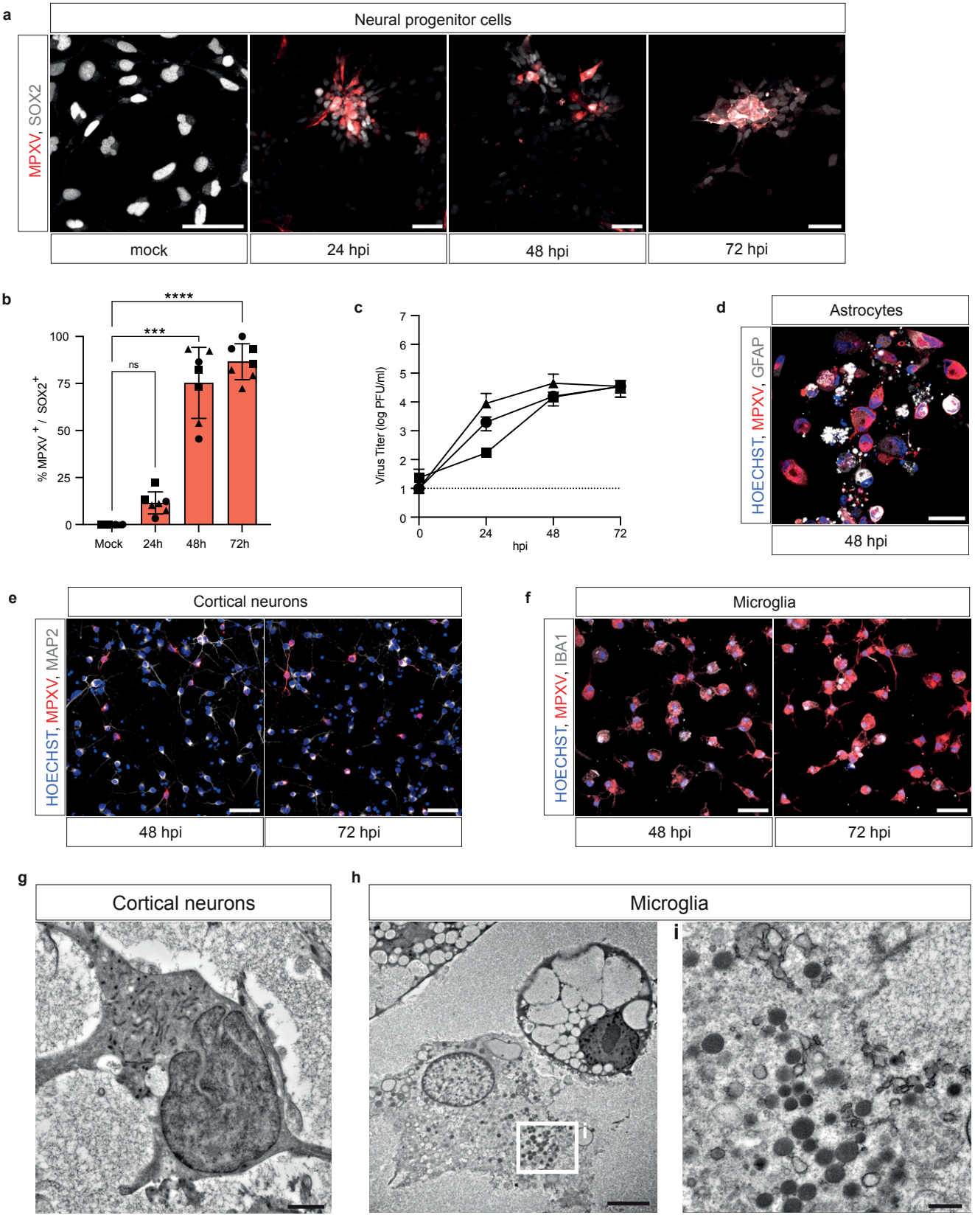

Supplementary figure 4

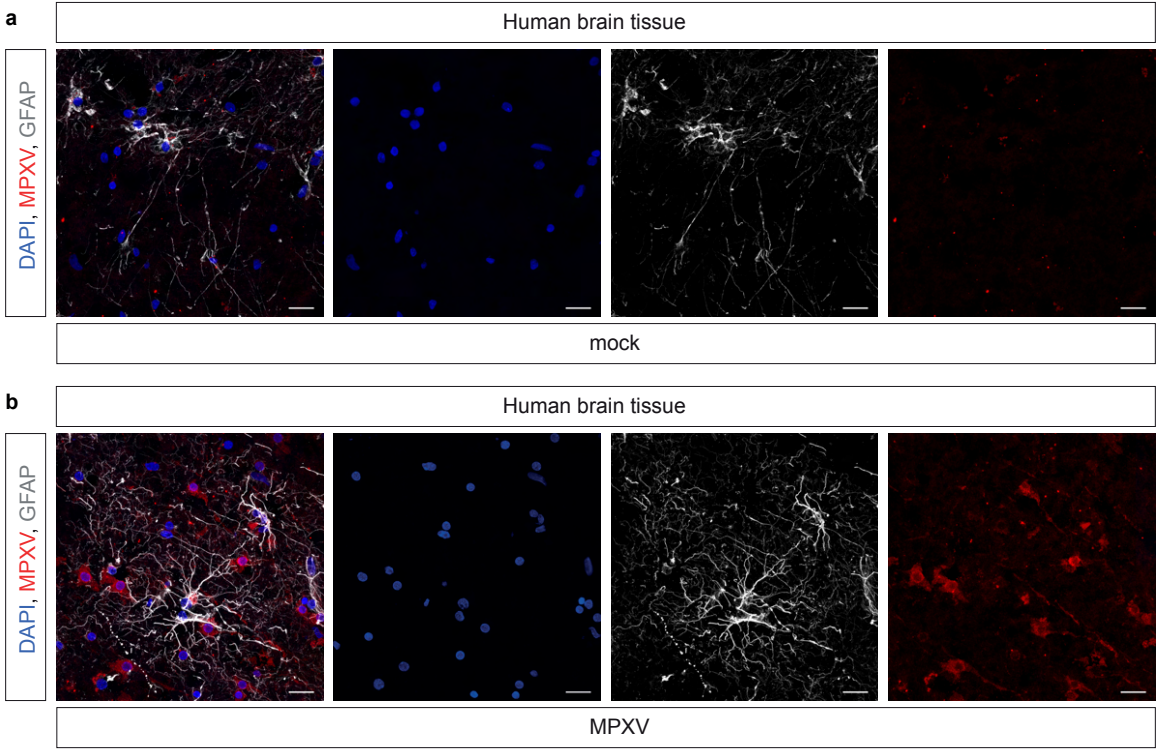

Supplementary figure 5

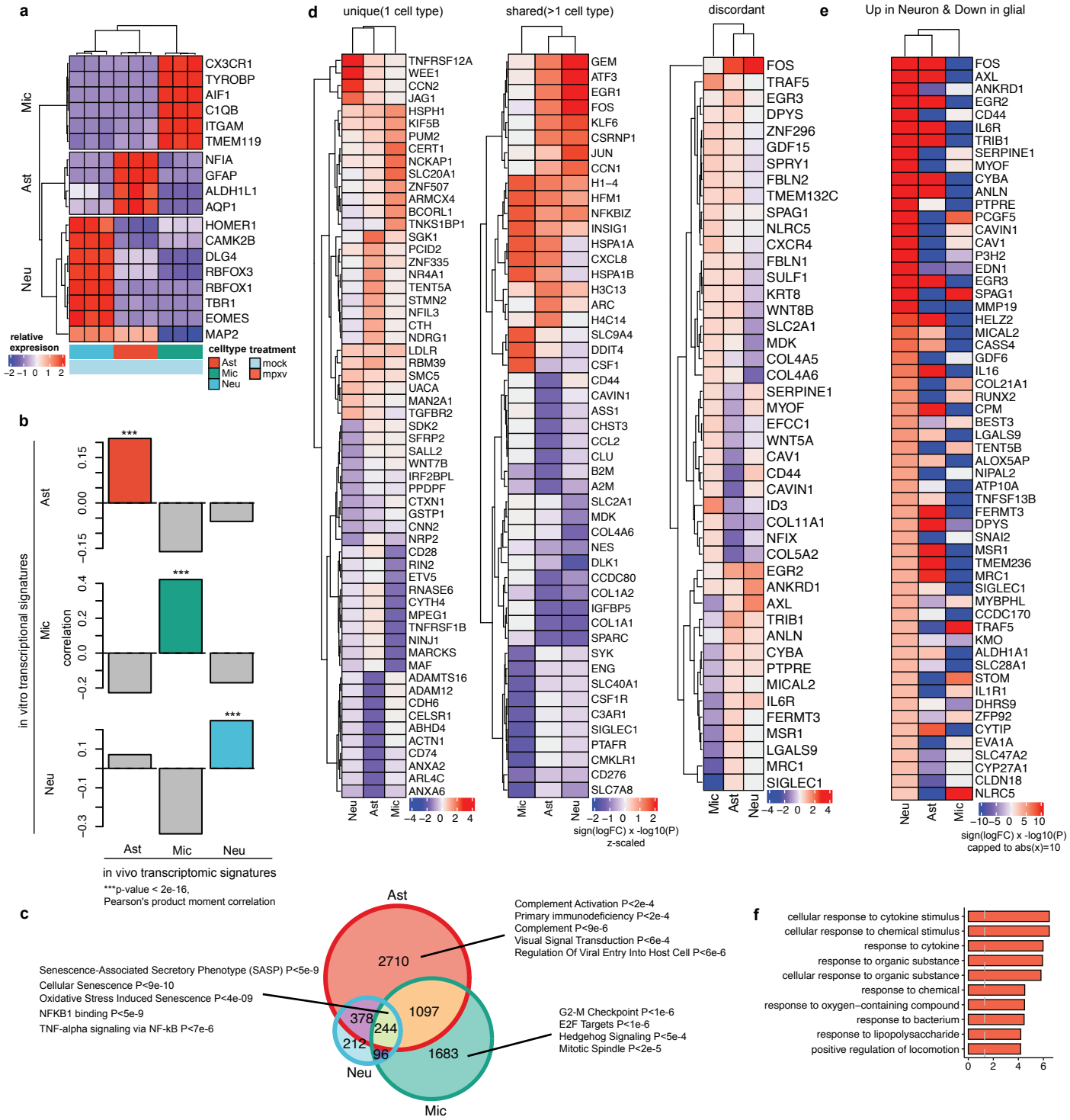
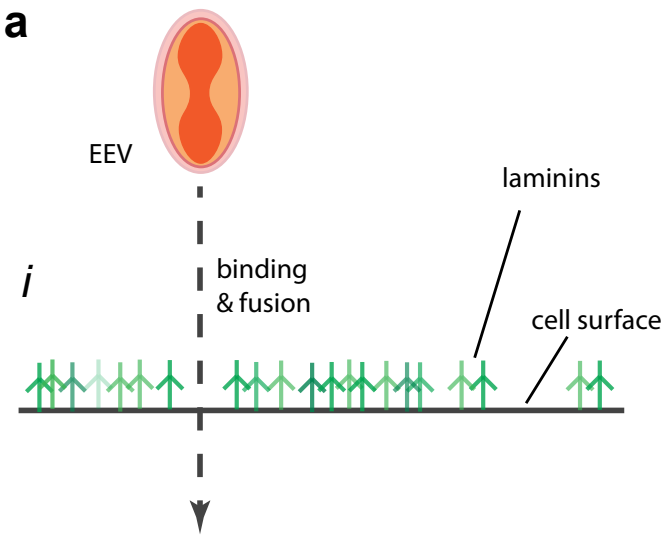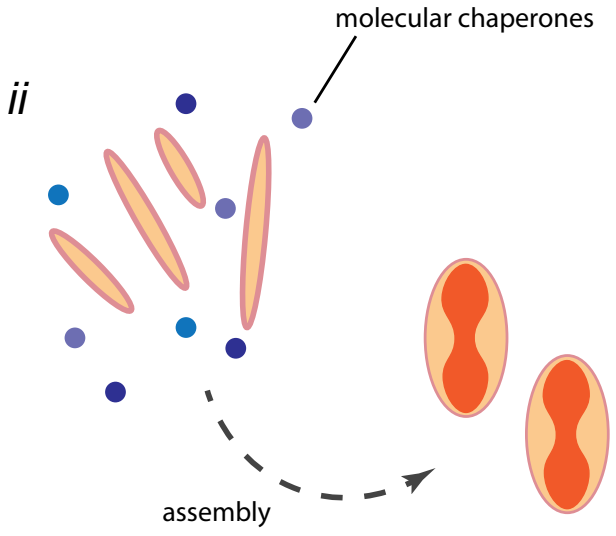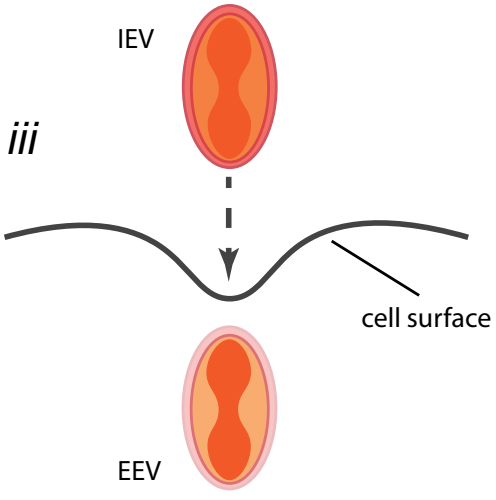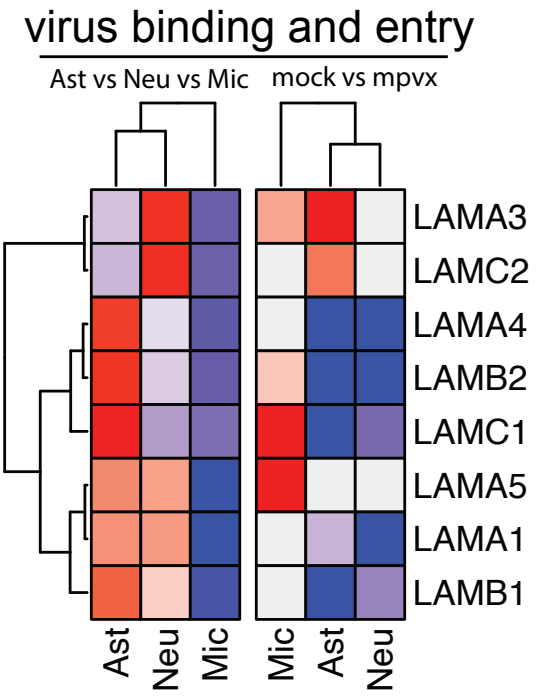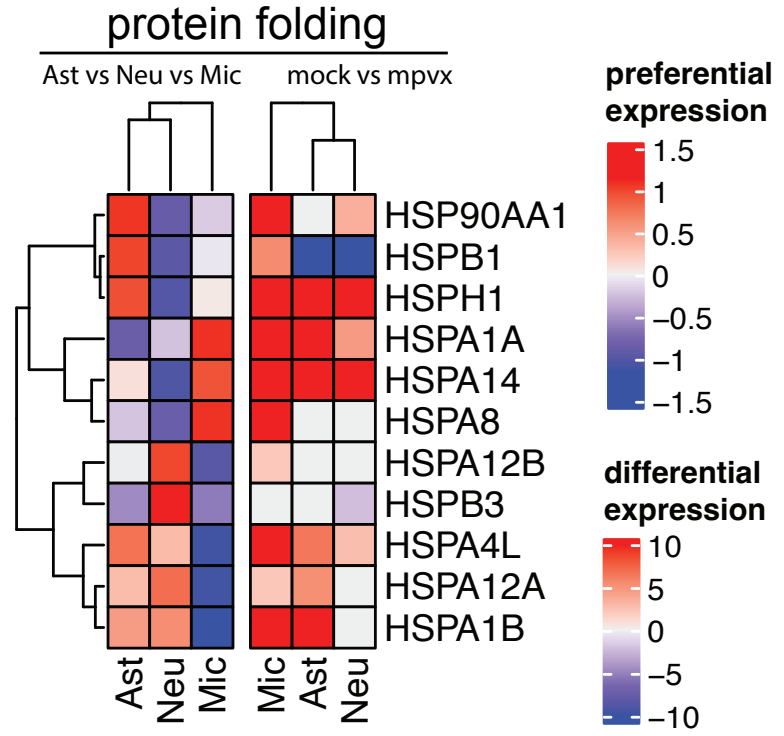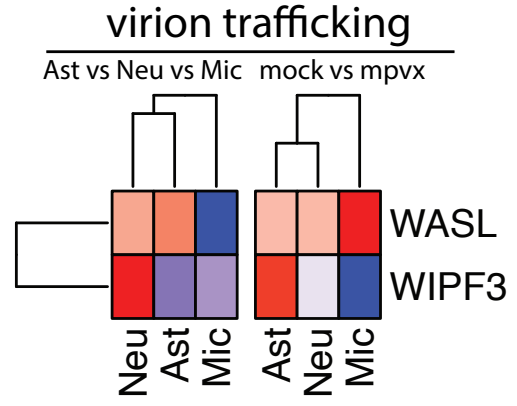
Supplementary figure 6